Annu. Rev. Mater. Res. 2008.38:559-584. Downloaded from arjournals.annualreviews.org
by UNIVERSITY OF WASHINGTON - HEALTH SCIENCES LIBRARIES on 10/21/08. For personal use only.

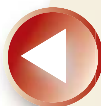

ANNUAL REVIEWS Further
Click here for quick links to Annual Reviews content online, including:
• Other articles in this volume
• Top cited articles
• Top downloaded articles
• Our comprehensive search

Transmission Electron Microscopy of Multilayer Thin Films*

Amanda K. Petford-Long[†] and Ann N. Chiaramonti

Materials Science Division, Argonne National Laboratory, Argonne, Illinois 60439;
email: petford.long@anl.gov, chiaramonti@anl.gov

Annu. Rev. Mater. Res. 2008. 38:559–84

First published online as a Review in Advance on April 7, 2008

The *Annual Review of Materials Research* is online at matsci.annualreviews.org

This article's doi:
10.1146/annurev.matsci.38.060407.130326

Copyright © 2008 by Annual Reviews.
All rights reserved

1531-7331/08/0804-0559$20.00

*The U.S. Government has the right to retain a nonexclusive, royalty-free license in and to any copyright covering this paper.

[†]Corresponding author.

Key Words

interfaces, microstructure, confinement effects, layered structures, characterization

Abstract

The unique geometry of multilayer thin films, with layer thicknesses on the nanoscale, gives rise to a wide range of novel properties and behavior that are not observed in the bulk. The novel behavior is critically dependent on the microstructure of the films. This paper reviews the use of a range of transmission electron microscopy (TEM) techniques to elucidate the structure, chemistry, and properties of multilayer thin films. The paper includes a brief introduction to the technological applications to which multilayer thin films are suited, followed by a description of the various TEM techniques. The final section of the paper presents the application of these techniques to various multilayer thin film systems.

Annu. Rev. Mater. Res. 2008.38:559-584. Downloaded from arjournals.annualreviews.org
by UNIVERSITY OF WASHINGTON - HEALTH SCIENCES LIBRARIES on 10/21/08. For personal use only.

1. INTRODUCTION

MTJ: magnetic tunnel junction

GMR: giant magnetoresistance

There has been intense interest in the development of multilayer thin films over the past few decades, both because of the fundamental properties that such films display and because of their potential (and indeed actual) use in a range of diverse technological applications. For the purposes of this review, the term multilayered thin film refers to both structures composed of many repeats of two alternating layers, as well as structures composed of a stack of different layers. In all cases the thicknesses of the layers in the structures discussed here are on the order of a few nanometers down to a single monolayer. The unique properties of multilayered films arise when the repeat distance of the layers (or the layer thicknesses for a stack of different layers) becomes comparable to a characteristic length of some physical property, for example, the electron mean free path for electrical resistivity or the exchange interaction length for magnetic materials. The exact origin of the novel properties can be better defined with reference to the following list:

1. thin film effects resulting from the limited thickness of the materials, as, for example, in quantum tunneling through the oxide barrier in a magnetic tunnel junction (MTJ) (1), or the formation of discrete energy levels in GaAs/AlGaAs quantum well heterostructure lasers (2);
2. interface effects arising from the interactions between adjacent layers, for example, the exchange-biasing effect in which an antiferromagnetic layer affects the magnetization reversal behavior of an adjacent ferromagnet (3);
3. coupling effects between layers of the same type separated by an intervening layer, for example, the observation in Fe/Cr multilayers of antiferromagnetic alignment of the magnetization in the Fe layers that leads to the giant magnetoresistance (GMR) effect (4); and
4. effects that arise from the overall periodicity of the multilayer, for example, the formation of high-quality X-ray mirrors from repeated stacks of high-atomic-number and low-atomic-number elements such as La/B_4C or W/Si (5), or the formation of nonequilibrium phases through annealing multilayer films of the constituent phases (6).

Combinations of these effects give further breadth to the properties that multilayer thin films can display—for example, the wavelength that is reflected by an X-ray mirror is controlled by the thickness of the layers and the angle of the incident X-ray beam, and the reflectivity and quality of the reflected X-rays are controlled by the number of repeats in the multilayer.

The fact that multilayer thin films can be grown by combining many different materials, with the resultant properties depending on the materials from which their constituent layers are composed and on the layer thickness, has led to their application in many fields of nanotechnology. These are briefly reviewed here. The earliest application of multilayered films was in semiconductor heterostructures such as GaAs/AlGaAs quantum well lasers, and many books and review articles address this technology (see, e.g., Reference 7). Developments in semiconductor multilayer structures have continued; some examples are the vertical-external-cavity-surface-emitting laser (8), quantum cascade lasers consisting of multiple quantum wells in a superlattice (9), and Si/SiO_2 superlattices in which confinement of the Si in thin layers leads to optoelectronic applications (10). Semiconductor and chalcogenide alloy superlattices are also of interest for thermoelectric applications and have shown excellent thermoelectric figures of merit (11). In the case of Si/SiGe superlattices, the high thermoelectric figure of merit is a result of an enhanced thermoelectric power factor (Seebeck coefficient squared times electrical conductivity), whereas for chalcogenide alloy superlattices such as Bi_2Te_3/Sb_2Te_3, the high thermoelectric figure of merit arises because phonon scattering at the interfaces reduces the thermal conductivity more than the electrical conductivity (12). Chalcogenide alloy layers are also the material of choice for phase-change storage media, and recent developments have led to the use of so-called superlattice media, consisting of

alternating layers of two phase-change alloys, one of which has a high crystallization rate and the other of which has high stability (13).

X-ray optical elements consisting of alternate layers of high atomic number and low atomic number are in use in a wide range of X-ray instruments for applications such as monochromators and mirrors (5). The thicknesses of the layers are chosen so that the X-rays reflected from each interface add nearly in phase. This gives rise to a very high overall reflectivity, at a wavelength that can be fine-tuned by tilting the multilayer element with a small angle with respect to the incident beam. In addition, the ability to deposit the multilayer films on curved substrates, and with a lateral layer thickness profile, enables the design of optical elements that can actually shape the X-ray beam. A further application of multilayer films is for hard coatings, in which alternating layers of, for example, TiN and TaN are combined to give rise to mechanical properties superior to those of the constituent materials (14). This effect is believed to result from the increased difficulty of motion of dislocations, as a result of a difference in shear stiffness of the two components (15). Many other possible materials combinations for which the origin of the increase in hardness is different can be used—for example, the use of TiN to stabilize a material such as AlN in the fcc phase (as opposed to the usual hexagonal phase) by confining the AlN in thin layers within a multilayer structure (16). A further advantage of multilayer hard coatings such as TiN/TiB_2 is that they can show enhanced thermal stability, an important consideration for high-temperature applications (17).

MBE: molecular beam epitaxy

PLD: pulsed laser deposition

As mentioned above, an important development in magnetic nanostructures was the observation of the GMR effect in magnetic/nonmagnetic multilayer films. This has led to the development of spin valves and MTJs, which have applications as field sensors, read-heads, and memory (18). Ferroelectric multilayers also have applications in memory (19) as well as in nanoelectromechanical systems and in optoelectronic devices (20). Ferroelectric random access memory nanocapacitors typically consist of a layer of a ferroelectric perovskite such as $SrBiTiO_3$ sandwiched between electrodes, which can be metallic (e.g., Pt) or a conducting oxide, such as $SrRuO_3$. Properties of the ferroelectric layer, such as polarization domain size, are controlled by the surface polarization, which in turn is strongly influenced by the interfaces with the electrodes. Multilayer and superlattice films are also of considerable interest as model systems in which to study confinement and interface effects as related to novel electronic, magnetic, and physical properties. One example of this is epitaxial magnetic oxide superlattices in which exchange coupling and exchange bias are being studied (21).

Improvements in growth techniques such as sputter deposition, molecular beam epitaxy (MBE), pulsed laser deposition (PLD), and atomic layer deposition (22, 23) have led to the routine deposition of layers as thin as a single monolayer, with the ability to build up complex stacks of different layers such as those discussed above. The structural properties of the multilayers are often complex, combining amorphous and polycrystalline layers, as produced most often by sputter deposition and PLD, or epitaxial layers, as produced by MBE. In all cases, the properties of the multilayer film depend critically on the nanostructure of the constituent layers, for example, whether the layers are polycrystalline or single crystal, or crystallographically textured or with random grain orientations, and in particular on the interfaces between the layers. The contribution of the interfaces to the properties cannot be stressed too strongly—the presence of roughness or interdiffusion between the layers can have a drastic effect on properties. One example of this is the degree to which spin flip is observed in magnetic multilayers: The thickness of the layers relative to the spin diffusion length controls the probability of spin flip within a ferromagnetic layer, and the quality of the interfaces on either side of the layer affects the degree of spin flip that is observed at the interfaces (24). It is therefore critical that characterization techniques are used with a resolution that is appropriate to the length scales of interest, both across the interfaces and along the length

Annu. Rev. Mater. Res. 2008.38:559-584. Downloaded from arjournals.annualreviews.org
by UNIVERSITY OF WASHINGTON - HEALTH SCIENCES LIBRARIES on 10/21/08. For personal use only.

Annu. Rev. Mater. Res. 2008.38:559-584. Downloaded from arjournals.annualreviews.org
by UNIVERSITY OF WASHINGTON - HEALTH SCIENCES LIBRARIES on 10/21/08. For personal use only.

of the layers. Both the structure and the composition profile need to be understood at the local scale, and to this end the remainder of this article addresses the contribution that transmission electron microscopy (TEM) is making to the study of multilayer thin films. Section 2 presents the various experimental TEM techniques of interest, and Section 3 provides examples of the way in which TEM characterization has been applied to multilayer materials systems, with the aim of giving the reader an idea of what is possible with this powerful technique.

TEM: transmission electron microscopy

XRD: X-ray diffraction

HREM: high-resolution electron microscopy

EFTEM: energy-filtered transmission electron microscopy

EELS: electron energy loss spectroscopy

2. EXPERIMENTAL TECHNIQUES

The investigation of multilayered thin films requires specialized experimental techniques that must cover a wide range of properties, both chemical and physical, and with very high spatial resolution. In a typical experiment, it is important to ascertain some combination of the following parameters: layer thickness, crystallographic orientation in and out of the plane of the films, short- or long-range order, epitaxy with the substrate and other layers, grain size and orientation, physical roughness, chemical interdiffusion, and atomic-scale structure and defects. In addition, it may even be necessary to know the oxidation state and bonding environment of the individual atoms. Neutrons, photons, and electrons are all capable of obtaining much of the aforementioned information, but TEM is unique in its ability to combine real- and reciprocal-space information from the same spatial location and at very high resolution. Electrons interact more strongly with matter than do neutrons or photons and can readily lose energy in the interaction. This means that, like neutrons and photons, electrons are sensitive not only to structure but also to chemistry such as local bonding environment and oxidation state. However, the real strength of electrons is that they can be focused into a much finer probe and can therefore provide such chemical information on a finer local scale.

Although TEM methods are very useful for the investigation of multilayer thin films, they do have some drawbacks and are at their most powerful and flexible when combined with complementary methods such as neutron and photon scattering (25–27), three-dimensional atom probe tomography (28), and ion- and photon-based spectroscopies, to name a few. Some drawbacks of TEM-based methods (29) are the small field of view leading to small sampling size, the possibility of electron beam–induced damage, destructive and time-consuming specimen preparation techniques, and difficulty of image interpretation. In addition, a high degree of user input is required because TEM cannot easily be automated as is the case in, for example, the collection of powder X-ray diffraction (XRD) data. This section concentrates on the various experimental techniques available in the transmission electron microscope for investigating thin film multilayers, including high-resolution electron microscopy (HREM), transmission electron diffraction, energy-filtered imaging (EFTEM) and electron energy loss spectroscopy (EELS), electron holography, and atomic-number-contrast (*Z*-contrast) imaging. Readers interested in general TEM techniques should refer to the classic texts for reference (29–32).

2.1. High-Resolution Electron Microscopy

HREM is one of the most common and widely used experimental techniques in TEM. For excellent reviews of HREM experimentation, image contrast, and interpretation, see References 33 and 34. An HREM image is formed in the image plane (as opposed to the back focal plane, which contains reciprocal-space information, i.e., the diffraction pattern) when two or more Bragg-reflected beams, selected by a suitably large objective aperture, interact (interfere) to form an image. Because the contrast arises from the difference in phase of the beams as a result of their interaction with the specimen, HREM imaging is a type of phase-contrast imaging and can be used

Annu. Rev. Mater. Res. 2008.38:559-584. Downloaded from arjournals.annualreviews.org
by UNIVERSITY OF WASHINGTON - HEALTH SCIENCES LIBRARIES on 10/21/08. For personal use only.

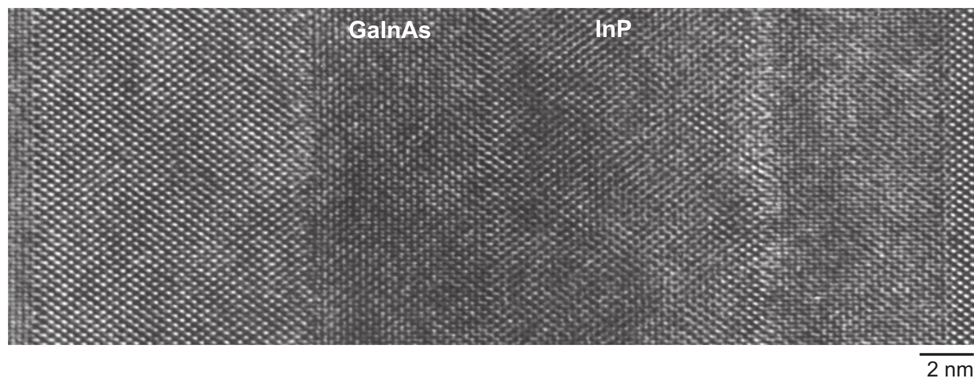

Figure 1

HREM image of InP/GaInAs quantum well structure. The layers can be distinguished by the difference in image contrast that they display, despite having the same crystal structure.

to resolve the crystalline lattice, columns of atoms, or, in the case of the most modern aberration-corrected transmission electron microscopes, sub-Ångström imaging of the lattice (35) and even single atoms (36). For the case of interfaces in multilayer thin films, HREM imaging can readily reveal crystalline defects, second-phase or amorphous layers, and atomic-resolution structure across boundaries, as well as information on the topography of the interface, provided that it is properly aligned in the direction of the electron beam. Although HREM images are relatively easy to obtain, their analysis is complicated and can often require simulation to directly interpret the contrast present in the image. For example, **Figure 1** shows an HREM image of an InP/GaInAs quantum well structure in which the layers have the same crystal structure and are lattice-matched. The positions of the layers can be clearly seen because the difference in scattering factor for a given Bragg reflection between the two materials, and the fact that the image contrast is formed from interference of these various reflections, leads to a difference in appearance of the crystal lattice for the two materials. However, at the resolution with which this image was recorded, the bright and dark dots in the image cannot be interpreted directly in terms of the atomic columns. The sample thickness, the imaging conditions, and physical constants of the microscope such as the chromatic and spherical aberration constants (C_c and C_s, respectively) all influence the image contrast. HREM image simulation packages have become highly developed, however, and many popular packages are available on the Internet free of charge (e.g., **http://www.numis.northwestern.edu/edm, http://cecm.insa-lyon.fr/CIOL/**).

2.2. Transmission Electron Diffraction

A transmission electron diffraction pattern is formed in the back focal plane of the objective lens of the transmission electron microscope and represents, in its simplest form, the Fourier transform of the specimen object. The diffraction pattern can be thought of as a magnified view of a slice through the reciprocal lattice of the specimen along a particular crystallographic direction. For a recent and thorough treatment of diffraction in the TEM, see Reference 37.

Incident electrons are scattered by the full electrostatic potential of a specimen (as opposed to the charge density, as is the case for X-rays), and in certain directions these scattered waves or beams are in phase because they satisfy the Laue conditions for diffraction. The Laue conditions for diffraction in the TEM are relaxed when compared with the case of XRD, because of the higher

Annu. Rev. Mater. Res. 2008.38:559-584. Downloaded from arjournals.annualreviews.org
by UNIVERSITY OF WASHINGTON - HEALTH SCIENCES LIBRARIES on 10/21/08. For personal use only.

STEM: scanning transmission electron microscopy

HAADF: high-angle annular dark field

CTEM: conventional transmission electron microscopy

energies used in TEM (typically 100–1000 keV) and the finite thickness of the specimen (typically $<$100 nm) in the direction of the electron beam. The relaxation of the Laue conditions means that diffraction occurs even when the Bragg condition is not exactly satisfied, and so many diffracted beams can be present in the diffraction pattern for a given alignment along the beam direction. Similar to XRD, however, the position and intensity of a particular diffraction peak (spot) depend on the scattering atoms and their position in the crystal. Because diffraction patterns represent the amplitude component of the Fourier transform of the projected potential of the specimen, they contain information about, and can be used to analyze, crystalline defects, long- and short-range order, orientation relationships between two phases or layers, superlattice periodicity, and the nature of additional phases present, for example, at the interfaces.

2.3. *Z*-Contrast Imaging

In a traditional TEM experiment, the electron beam illuminates the specimen uniformly, and all image capture is in a parallel mode. Scanning transmission electron microscopy (STEM), as its name suggests, is a modification of the normal technique in which a nanometer-sized electron beam is rastered or scanned point by point across the specimen. Although the details of the STEM optical system are beyond the scope of this review (see References 38 and 39), the detector in a STEM microscope makes it possible to exclude electrons scattered at low angles (coherent Bragg scattered) and collect only the electrons incoherently scattered at very high angles ($>$50 mrad). This is accomplished practically by using an annulus-shaped detector with a large hole in the center to exclude coherently diffracted beams scattered at low angles. Such a detector is aptly named a high-angle annular dark-field detector, and the images formed from the incoherently scattered electrons are known as high-angle annular dark-field (HAADF) images. A HAADF image, lacking diffraction contrast and having very little if any phase contrast, contains intensity proportional to the square of the atomic number (Z) of the scattering atom according to the Rutherford scattering equation and is therefore also known as a Z-contrast image. Because the image intensity is dependent only on the atomic number and thickness of the sample, the images can, in most cases, be interpreted directly, and chemical concentrations of heavy species can be accurately estimated. In a standard HREM image, there can be very little contrast between layers of similar composition. In the HAADF image, however, the two phases can be readily identified, as in the case of GaN/AlGaN layers in a violet laser diode (40). HAADF imaging is also very useful for examining small concentrations of high-Z atoms in a light-element matrix, which is very common in catalysis applications. **Figure 2** shows a HAADF image of a Ta/IrMn/$Co_{90}Fe_{10}$/TiO_x/$Co_{90}Fe_{10}$ MTJ structure. The dark (low-atomic-number) tunnel barrier can be clearly seen.

Conventional transmission electron microscopy (CTEM) can also be used for Z-contrast imaging, although such images will always contain some diffraction contrast because Bragg-scattered beams cannot be eliminated entirely from contributing to the image. This is because the electron optical system in a CTEM is different from that of a STEM [in fact, the electron paths are exactly reciprocal to each other (39)], and to totally eliminate diffraction contrast in CTEM, very large beam convergence angles are required, which would be difficult if not impossible to achieve without significant modifications to the illumination system. Nevertheless, images displaying Z-contrast can be obtained in CTEM by using the highest possible beam convergence angle and excluding the low-angle scattered beams; the latter is accomplished by the use of a detector with a small hole in the center. This type of detector is simply called an annular dark-field detector, and CTEM annular dark-field images can display contrast similar to that of a true STEM-HAADF image (41).

Annu. Rev. Mater. Res. 2008.38:559-584. Downloaded from arjournals.annualreviews.org
by UNIVERSITY OF WASHINGTON - HEALTH SCIENCES LIBRARIES on 10/21/08. For personal use only.

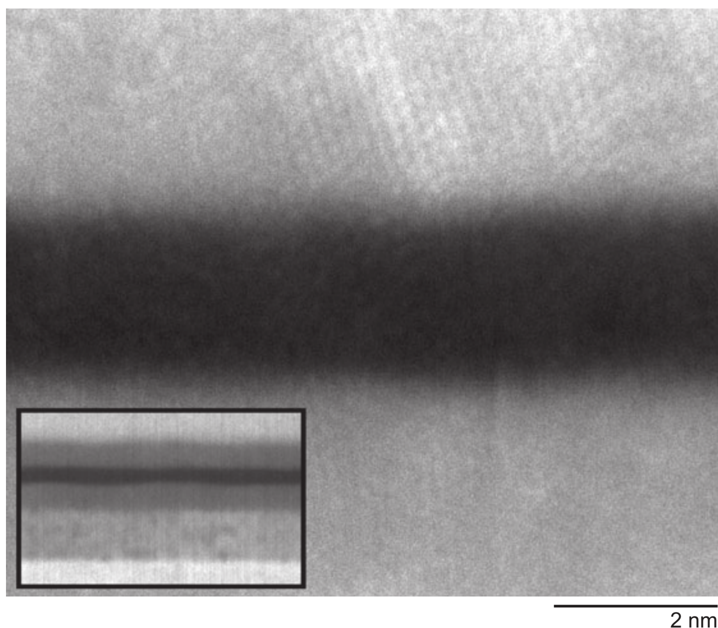

Figure 2

HAADF (*Z*-contrast) image of a CoFe/TiO_x/CoFe magnetic tunnel junction. The TiO_x tunnel barrier appears dark in the image because of its relatively low atomic number compared with the ferromagnetic metal electrodes and the underlying IrMn antiferromagnet. In the enlargement of the area inside the white rectangle, the atomic planes in the CoFe ferromagnetic layers can clearly be seen, as can the difference in contrast between all the layers as a result of the difference in atomic number. Images courtesy of D. Kirk, University of Oxford.

2.4. Energy-Filtered TEM/Electron Energy Loss Spectroscopy

In their interaction with a specimen, electrons scatter both elastically and inelastically. Elastically scattered electrons are the primary basis for imaging and diffraction in the TEM, whereas inelastically scattered electrons are the basis for EELS and EFTEM. The energy spread of inelastically scattered electrons in a TEM experiment carries a wealth of chemical information on the electronic structure of the specimen, including both localized core levels as well as the outermost delocalized atomic orbitals. When an incident electron interacts with the specimen and loses a small amount of energy (typically $<$50 eV), it can reveal specifics such as the thickness of the specimen, valence-electron density, and surface and interface states through analysis of the plasmon losses. In addition, the high-loss region of the EELS spectrum (typically 50–1000 eV) can be used to analyze the atom type through analysis of characteristic ionization edge energies; elemental concentration and distribution from the integrated intensity of the edge, the chemical state, local structure, coordination, and bonding through analysis of the shape of the near-edge structure; and bond distances through the analysis of the extended energy loss fine structure (42, 43). The combination of high spatial resolution and high energy resolution of EELS in a TEM is unique, and state-of-the-art aberration-corrected transmission electron microscopes have recently been used for single-atom spectroscopy (35).

Inelastically scattered electrons of a specific and usually narrow range of energy corresponding to characteristic inner shell ionizations can be selected by an in-line spectrometer and used to form an image through EFTEM imaging. Such an image represents a two-dimensional map of

Annu. Rev. Mater. Res. 2008.38:559-584. Downloaded from arjournals.annualreviews.org
by UNIVERSITY OF WASHINGTON - HEALTH SCIENCES LIBRARIES on 10/21/08. For personal use only.

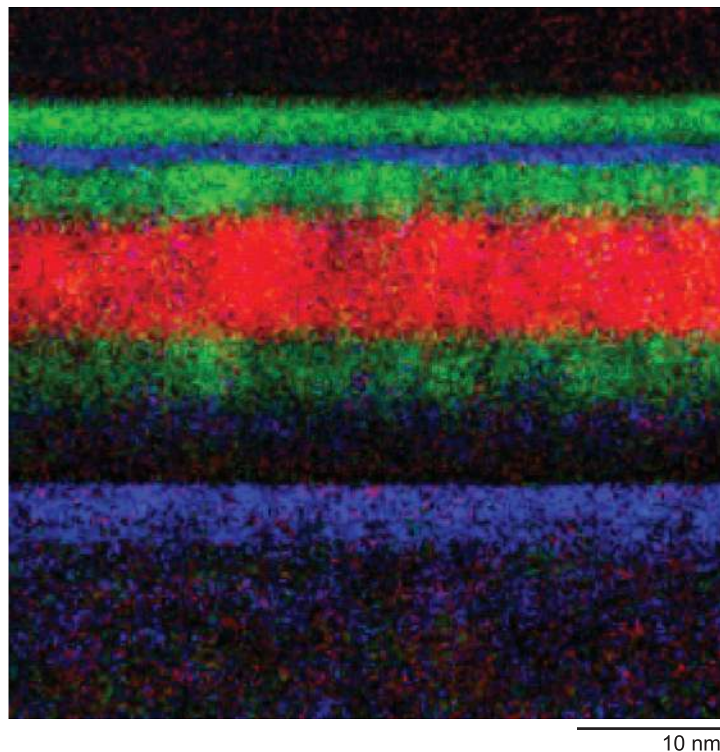

Figure 3

EFTEM image of a $Ta_{5nm}/NiFe_{6nm}/MnFe_{10nm}/NiFe_{4nm}/AlO_x/NiFe_{8nm}/Ta_{5nm}$ magnetic tunnel junction structure. The image is a composite prepared by superimposing the EFTEM images recorded using the Mn *L*-edge (*red*), the O *K*-edge (*blue*), and the Ni *L*-edge (*green*) and maps the projected spatial distribution of each element. It is essentially a two-dimensional map of the distribution of each element in the sample. Image courtesy of P. Shang, University of Oxford.

the selected element within the sample. Variations of this general technique can be used to form thickness maps, chemical state maps, and so-called three-dimensional spectrum images, in which each pixel in an image is associated with a full energy spectrum.

For multilayer thin films, EELS and EFTEM imaging are indispensable techniques and have been used to analyze the chemistry of single atomic columns across a phase boundary (44), asymmetry in oxygen bonding between the top and bottom ferromagnet interfaces in MTJs (45), and energy loss spectra specifically from interfacial regions (46, 47), to name a few examples. For a recent review of analytical TEM techniques in this journal, see Reference 48. An EFTEM image of a $Ta_{5nm}/NiFe_{6nm}/MnFe_{10nm}/NiFe_{4nm}/AlO_x/NiFe_{8nm}/Ta_{5nm}$ MTJ structure is shown in **Figure 3**. The position of the thin AlO_x tunnel barrier between two NiFe layers can clearly be seen, as can the positions of the antiferromagnetic MnFe layer and the lower NiFe layer. The lower oxygen layer is at the position of the native oxide at the surface of the Si substrate. For more details of the sample, see Reference 49.

2.5. Phase-Retrieval Techniques

In electron holography, a sufficiently coherent source of electrons is "split" in the field of view. One portion of the beam (object beam) is allowed to interact with the specimen and so shifts

Annu. Rev. Mater. Res. 2008.38:559-584. Downloaded from arjournals.annualreviews.org
by UNIVERSITY OF WASHINGTON - HEALTH SCIENCES LIBRARIES on 10/21/08. For personal use only.

in amplitude and phase, whereas the remainder of the beam (reference beam) passes unchanged through vacuum at either the specimen edge or a suitably located hole. If the reference and object beams are then recombined by applying a voltage to an electrostatic biprism, an electron hologram, which is an interference pattern superimposed onto a "normal" image, is formed. The spacing and width of the fringes in the interference pattern contain information not only on the amplitude but the phase of the electron wave. This is important because in most TEM experiments such as diffraction, bright-/dark-field imaging, EFTEM, and EELS, to name a few, the phase information is lost, and only the intensity (amplitude squared) of the complex electron wave is observable and recorded. If the phase information is also known, then the mean inner potential, magnetic induction, and magnetization can be obtained directly and quantitatively through Fourier reconstruction techniques (50). Although it is true that some phase information can be "backed out" from an HREM image or diffraction pattern (51), electron holography is one of the only techniques that gives the phase directly. Electron holography techniques are discussed in detail in the text of References 52–54.

TIE: transport of intensity equation

An alternative technique by which the phase change of the electron beam can be extracted so that phase maps can be constructed is through use of the transport of intensity equation (TIE) (55). The TIE relates the longitudinal derivative (along the beam direction) of the image intensity to the in-plane (normal to the beam direction) variations of the phase. Experimentally, the derivative of the image intensity in the beam direction is approximated by recording three images at different defocus values and then using these to reconstruct the phase map. For applications of this technique to mapping of magnetization in thin films using TEM, see References 56 and 57. The approach has been used very successfully to reconstruct the magnetic phase and has more recently been applied to HREM imaging (58).

2.6. In Situ Analyses: Dynamic Experiments and Analysis of Physical Properties

In many transmission electron microscopes, the objective (imaging) lens is a split electromagnetic immersion lens with a gap between the upper and lower pole pieces on the order of a few (3–5) millimeters. This means that the specimen holder (stage) is limited in size because it has to fit inside the small pole piece gap. Additionally, the specimen sits inside the lens and is subject to a large and fairly uniform vertical magnetic field on the order of 1–2 T. Until recently, the small size of the objective lens pole piece gap limited the types of in situ experiments that could be performed inside the TEM because of the limited space available for analytical instrumentation near the sample. Nevertheless, many in situ experiments have been conceived and successfully executed by the modification of the actual TEM stage as well as by making use of the magnetic field of the objective lens itself. Heating (59), cooling (60), strain (61, 62), nanoindentation (63), electron- and ion beam–induced irradiation damage (64), magnetization (65), and environmental reaction and growth studies (66, 67) have been successfully performed in situ. Recent advances in aberration correction have allowed for instrument designs with larger pole piece gaps (68), and the newest in situ TEM experiments are being conceived to include probes and detectors very close to the specimen. When combined with the newest fast electron guns and detectors (69), in situ dynamic studies inside of the TEM column will start to rival those performed at neutron and X-ray beam lines. Imaging the magnetic domain structure and following magnetization processes in situ in the TEM in magnetic thin films requires the specimen to be located in a controllable magnetic field and, in most cases, outside the high magnetic field of the objective lens. To achieve this, special Lorentz objective lenses have been designed: The specimen sits in a low magnetic field that can be increased, if desired, to follow a magnetization process in situ. Petford-Long & Chapman (70) have discussed various approaches to magnetic imaging.

Annu. Rev. Mater. Res. 2008.38:559-584. Downloaded from arjournals.annualreviews.org
by UNIVERSITY OF WASHINGTON - HEALTH SCIENCES LIBRARIES on 10/21/08. For personal use only.

3. APPLICATIONS TO MULTILAYER FILMS

EDX: energy-dispersive X-ray spectroscopy

This section presents examples of the applications of the various TEM techniques described in Section 2 to multilayer thin films. TEM has been widely used to study such materials, and it is therefore not possible to give a comprehensive overview of the literature in this field. The aim is rather to provide specific examples that highlight the strengths of the various techniques and the information that can be obtained by using them, with reference to a wide number of different materials systems. The subsections here include a discussion of the analysis of microstructure, composition, and physical properties, and, in addition, of the use of in situ techniques enabling the response of a specimen to a controlled environment to be probed.

3.1. Semiconductor Superlattices

In semiconductor heterostructures the multilayer film often can be considered as a single crystal in which the composition is modulated in a controlled manner to produce layers, as, for example, in InP/GaInAs quantum well laser structures. In other cases the layering is a result of physical deposition of adjacent materials with very different structures, as, for example, in transistor devices in which the gate oxide is often amorphous but with crystalline layers on either side. In all cases, however, the microstructure is critical in controlling the electronic structure of the heterostructure and thus its transport behavior and overall device performance. Early studies of semiconductor superlattices using TEM relied mainly on bright- and dark-field imaging, in which a single diffraction spot is used to form the image, and on electron diffraction; see, for example, a discussion of these techniques by Petroff (71). The alternating layers in, for example, a GaAs/GaAlAs superlattice could be clearly distinguished when imaging in dark field using a {200}-type diffraction spot because of the difference in atomic scattering factors and thus in structure factor for this reflection for the two materials. This translated to a difference in intensity in the image for the two materials. Another technique that relies on the difference in atomic scattering factors for different semiconductor materials is the wedge TEM technique (72–74). Imaging through a cleaved edge of the layered structure, using the undiffracted beam to form a bright-field image, results in a map of thickness fringe profiles, in which the thickness fringe spacing is a function of the local composition of the material. For example, in InGaAs/InP quantum well structures (75) the difference in interdiffusion width of the interfaces below and above the InGaAs quantum wells could be clearly distinguished and modeled through the use of the multislice approach (76). Composition profiles across a graded $Al_{0.5}Ga_{0.5}As$/AlAs multilayer, obtained via energy-dispersive X-ray spectroscopy (EDX) analysis and averaging of EFTEM images parallel to the interfaces, showed very good agreement with a model of the composition profile (77), indicating the excellent spatial resolution of the techniques.

Superlattices can be formed not only by alternate deposition of two different materials but also by spontaneous decomposition of alloy layers. Gao et al. (78) presented evidence for this latter phenomenon, using the HAADF imaging technique and EDX analysis to analyze the degree of interfacial diffusion between Ga-rich and Al-rich layers in an atomic compositional superlattice formed by spontaneous segregation of an AlGaN layer. HAADF imaging has replaced the {200} dark-field imaging technique; although the HAADF technique provides similar image contrast, it offers much improved spatial resolution. A further novel method by which multilayer films can be formed is to produce a strained-layer film on a substrate and then release the film so that the layers roll up and produce a radial superlattice (79). Deneke et al. (80) used HREM, HAADF imaging, EDX, and EELS analysis to study the microstructure and composition profile in InAlGaAs/GaAs/Cr and InGaAs/Ti/Au radial superlattices. These systems do not show coherent

Annu. Rev. Mater. Res. 2008.38:559-584. Downloaded from arjournals.annualreviews.org
by UNIVERSITY OF WASHINGTON - HEALTH SCIENCES LIBRARIES on 10/21/08. For personal use only.

crystal structure across all the layers because they are effectively formed from a single repeat of the layering. The HAADF and HREM images of the InGaAs/Ti/Au system showed small voids and interfacial roughness at the Au/InGaAs interfaces, as might be expected from the preparation method. However, the Cr/InAlGaAs interfaces are smooth and show no voids, indicative of good cohesion between the adjacent repeats of the structure. A further application of the HAADF technique for analysis of semiconductors is in electron tomography, which has been used very effectively to produce a three-dimensional reconstruction of a flash memory cell containing many layers: poly-Si gates, SiO_x, Ti silicide, Si nitride, and W. These data could be used to visualize the interfacial roughness in the device, albeit at a reduced resolution (of the order of 1 nm) compared with the HAADF data discussed above in this section (81).

HREM imaging can be used very effectively to show the degree of interfacial roughness in semiconductor heterostructures, as, for example, in the study by Gribelyuk et al. (82) of $NiSi_x/HfO_2/SiO_x/Si$ and poly-Si/HfO_x/SiO_x/Si gate structures being developed for use in MOSFET devices. The $NiSi_x/HfO_x$ interfaces were observed to be rougher than the equivalent poly-Si/HfO_x interfaces, but EELS and EDX analysis showed no evidence for chemical interdiffusion. The image detail observed in HREM images of crystalline alloy semiconductor materials is more complex and depends critically on defocus, sample thickness, and other microscope parameters. This has to be taken into consideration when interfacial mixing is analyzed, as shown by the variation in interface contrast for diffuse interfaces in InP/GaInAs superlattices (83), for which the apparent position of the interface can vary considerably as a function of defocus and thickness. The use of an aberration-corrected TEM can greatly reduce this effect, as shown by Lentzen et al. (84) for GaAs/AlAs/GaAs heterostructures.

Semiconductors, like all TEM specimens, are susceptible to electron beam irradiation damage over the course of examination. Although in most cases beam damage has a deleterious and unwanted effect on the specimen, Smeeton et al. (85) used beam damage to their advantage in studying the effect of irradiation damage induced by 200–400-kV electron beams in $In_xGa_{1-x}N$/GaN quantum wells. In that work, inhomogeneous strain was detected by measuring the local variation in the (002) lattice fringe spacing. The investigators showed that the strain associated with even a brief period of electron irradiation could mimic the strain expected from nanometer-scale fluctuations in the Ir content of the layers. They concluded that care must be taken when examining these materials in TEM because they beam damage on the order of minutes. This work demonstrates the importance of accounting for electron beam damage in any TEM study, especially for materials that are particularly sensitive to electron beam damage, such as oxides.

It is often useful when analyzing semiconductor devices to understand the electrostatic potential profile across a multilayer junction, both in the biased and unbiased states. In the case of *p-n* heterojunctions, McCartney et al. (86) have used electron holography to determine the electrostatic potential variations across an unbiased diode (**Figure 4**). The energy profile of the diode was obtained after the electrostatic potential was converted to energy and the contribution was subtracted out from the mean-inner-potential offset. By comparing the experimental results with simulation, McCartney et al. were able to detect space charge regions with high spatial resolution and quantify the contributions of built-in voltage, spontaneous polarization, and piezoelectric polarization fields to the overall energy profile in an *n*-AlGaN/InGaN/*p*-AlGaN heterostructure.

Twitchett et al. (87) similarly used electron holography to measure the electrostatic potential across a reverse-biased Si *p-n* junction, for which the bias voltage was applied in situ in the TEM column through the use of a specialized electrical biasing holder. This particular specimen was not grown as a physical multilayer per se, but the dopant profiles combined with specimen preparation damage resulted in a chemically and electrically multilayered structure consisting of either a *p*- or an *n*-doped active layer surrounded symmetrically on both sides by an electrically dead crystalline

Annu. Rev. Mater. Res. 2008.38:559-584. Downloaded from arjournals.annualreviews.org
by UNIVERSITY OF WASHINGTON - HEALTH SCIENCES LIBRARIES on 10/21/08. For personal use only.

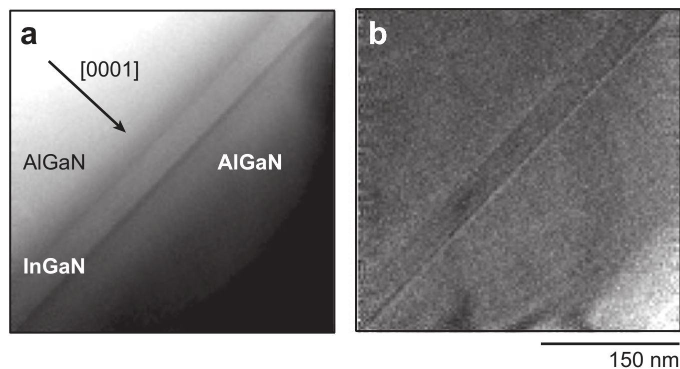

Figure 4

(*a*) Phase image and (*b*) amplitude image of an AlGaN/InGaN/AlGaN diode. The edge of the sample is at the lower right corner of the images, and the growth direction is indicated with an arrow in panel *a*. Images are courtesy of M.R. McCartney (Arizona State University) and reprinted with permission from Reference 86. Copyright 2000, American Institute of Physics.

layer and an outer electrically dead amorphous layer. This study showed that the thickness of the electrically dead layers and the width of the depletion region increased as the sample thickness was decreased, indicating that focused ion beam damage or proximity (thickness) effects were the cause. In either case, Twitchett et al. (87) put the minimum thickness to obtain useful measurement of the electrostatic potential in these particular devices at 350 nm, which is relatively thick for a TEM sample examined at low to intermediate voltages.

3.2. Spin Valves and Tunnel Junctions

One of the most important developments in magnetic nanostructures in recent years has been that of spin valves (88) and MTJs (89), which are based on the giant magnetoresistance (GMR) phenomenon (90). In their simplest form these devices are composed of three layers with thicknesses on the nanometer scale: two ferromagnetic layers separated by a nonmagnetic spacer, which is a metal in the case of spin valves and an oxide in the case of MTJs. Often, the structures contain many more layers, each of which contributes to the overall behavior of the structure. For example, the presence of an antiferromagnetic layer adjacent to one of the ferromagnetic layers pins its magnetization, such that in an applied field the angle between the magnetization in the two ferromagnetic layers can change independently. TEM has made a major contribution to the understanding of the microstructural origins of the magnetotransport in these structures, and the application of TEM techniques to the analysis of spin-valve materials was reviewed in 1999 (91). More recently, Song et al. (92) have presented a detailed comparison of the relative merits of using analytical TEM and X-ray reflectometry for measuring the tunnel barrier thickness in AlO_x-based MTJs, including a very valuable discussion of the limitations and advantages of the various techniques assessed. Song et al. concluded that TEM-EELS and STEM-EDX were the most powerful techniques available and that the quality of the various layers and of the interfaces between them is critical to controlling the magnetotransport behavior and thus needs to be understood at the atomic scale.

Figure 5*a* shows a cross-sectional HREM image of a spin-valve structure in which the layers are $Ta_{5nm}/NiFe_{6.5nm}/Co_{1.5nm}/Cu_{3nm}/Co_{2nm}/NiFe_{3nm}/MnNi_{25nm}/Ta_{5nm}$ (93). The grain structure and crystallographic texture can be clearly seen, with the grains showing a clear [111] texture along the growth direction. Of particular importance, however, is the morphology (i.e., structural roughness

Annu. Rev. Mater. Res. 2008.38:559-584. Downloaded from arjournals.annualreviews.org
by UNIVERSITY OF WASHINGTON - HEALTH SCIENCES LIBRARIES on 10/21/08. For personal use only.

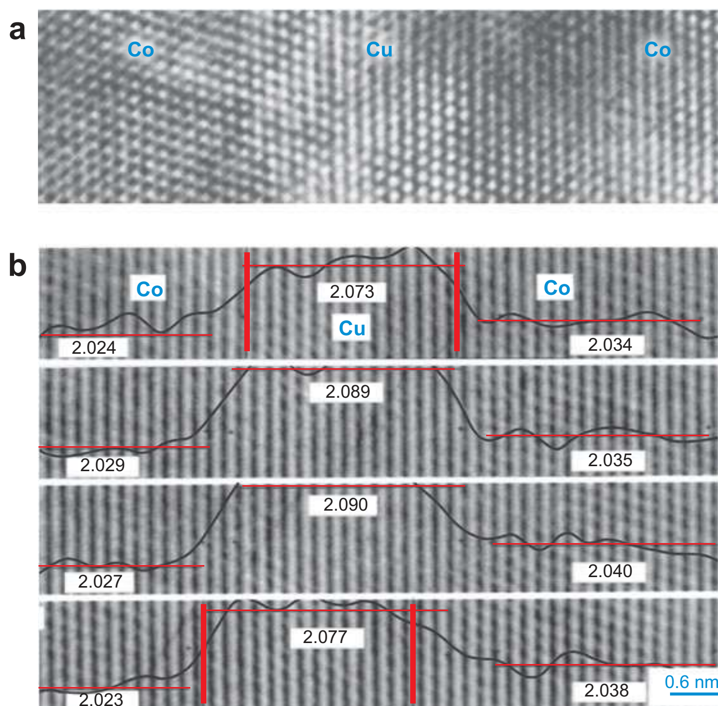

Figure 5

(*a*) HREM image of a NiFe/Co/Cu/Cu/NiFe/MnNi spin-valve structure and (*b*) a filtered region of the HREM image across the Co/Cu/Co layers. The superimposed line profile (*black*) traces the change in measured lattice spacing from the Co to the Cu layer and back. The thick red vertical lines indicate the positions at which the change occurs—note that these are displaced by three lattice planes (*thin red lines*) across the grain. Panel *b* is reproduced from Reference 93.

and chemical sharpness) of the interfaces between the ferromagnetic layers and the Cu spacer, and these are very difficult to distinguish from the image. **Figure 5*b*** shows a digitized section of part of the HREM cross section, following the technique developed by Rouvière (94) originally for analysis of semiconductor interfaces. The digitized regions are from different positions across a 15-nm-diameter grain, and superimposed are the profiles of the interplanar spacings. The profiles show a shift of approximately three ⟨111⟩ planes between the position of the interfaces at the edges of the grain and in the center. From these and similar data a measure of the amplitude and period of the waviness of the ferromagnet/Cu interfaces was determined. These parameters were then used to calculate the ferromagnetic "orange-peel" coupling between the two ferromagnetic layers (95), which was determined to be of the same order of magnitude (5 Oe) as the shift of the GMR curve with respect to zero field (93).

An HREM image of a MTJ with an amorphous AlO_x spacer layer (tunnel barrier) is shown in **Figure 6**. In this case, the difference between the oxide spacer layer and the ferromagnetic layers can be clearly seen because of the amorphous nature of the barrier and the lower average atomic number. As can be seen, the barrier is not completely flat, and there are regions where the lattice fringes corresponding to the ferromagnetic metal extend into the barrier region resulting from the projected roughness of the bottom ferromagnetic layer. These features highlight one of the issues that need to be addressed when one is making quantitative analysis of TEM images from multilayer films—namely that TEM (with the exception of electron tomography) is a projection

Annu. Rev. Mater. Res. 2008.38:559-584. Downloaded from arjournals.annualreviews.org
by UNIVERSITY OF WASHINGTON - HEALTH SCIENCES LIBRARIES on 10/21/08. For personal use only.

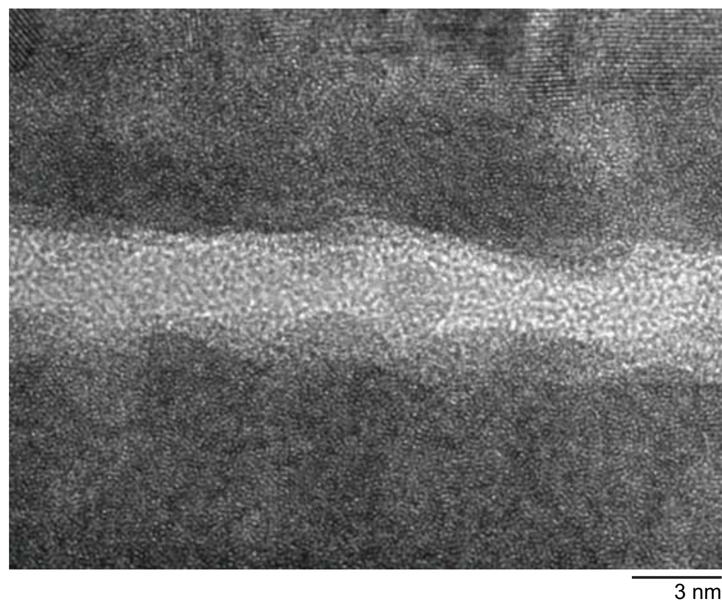

Figure 6

HREM cross-sectional image of a CoFeB/AlO_x/CoFeB magnetic tunnel junction structure. The AlO_x barrier (*light region*) does not show lattice fringe contrast, indicating that it is amorphous. Note that the ferromagnet/barrier interfaces are not flat and that the lattice fringes from the bottom ferromagnetic layer extend into the barrier, thus confirming roughness of the layer in the direction of the electron beam.

technique. Care must therefore be taken when imaging the interfaces in multilayer films when they are wavy or rough in the electron beam direction—as is likely to be the case for the film shown in **Figure 6**—given the general waviness along the sample parallel to the interface. Very useful qualitative information can be obtained, however, and correlated with, for example, the growth conditions used or the transport and magnetic properties.

More recent research on MTJs has concentrated on analysis of tunnel junction structures with MgO tunnel barriers because of the high tunneling magnetoresistance (TMR) that such structures were predicted to show (96). Here again, TEM has been widely used to reveal the microstructure of the layers and interfaces in the structures. For example, the first papers that presented experimental evidence of high TMR in MgO-based materials (97, 98) included TEM analysis, as do many more recent papers that discuss the further development of MgO-based structures (99, 100). **Figure 7*b*** shows an HREM image of an epitaxial Fe/MgO/Fe MTJ grown by MBE. As can be seen, the interfaces are flat, and the MgO tunnel barrier is clearly defined. As mentioned above, one of the important parameters that controls the behavior of the tunnel junction is the structure at the interfaces, which will affect the transport behavior of the device (101, 102). Panels a and c of **Figure 7** show simulations of the HREM images for two models of the Fe/MgO interface: one with a monolayer of Fe-O at the interface (103) and one without (104), both of which have been postulated in the literature. A cross-correlation of the experimental and simulated images showed that the sharp interface model (i.e., without the Fe-O) is a better match to the image (105). This then allows a more accurate model for the electronic structure at the interface to be determined.

TMR: tunneling magnetoresistance

TEM has also been used recently to investigate the barrier/electrode interfaces in CoFeB/MgO/CoFeB tunnel junction structures grown by different deposition techniques (45). Cha et al. (45) looked at details of the pre-edge structure in the O *K*-edge of the EELS spectrum

Annu. Rev. Mater. Res. 2008.38:559-584. Downloaded from arjournals.annualreviews.org
by UNIVERSITY OF WASHINGTON - HEALTH SCIENCES LIBRARIES on 10/21/08. For personal use only.

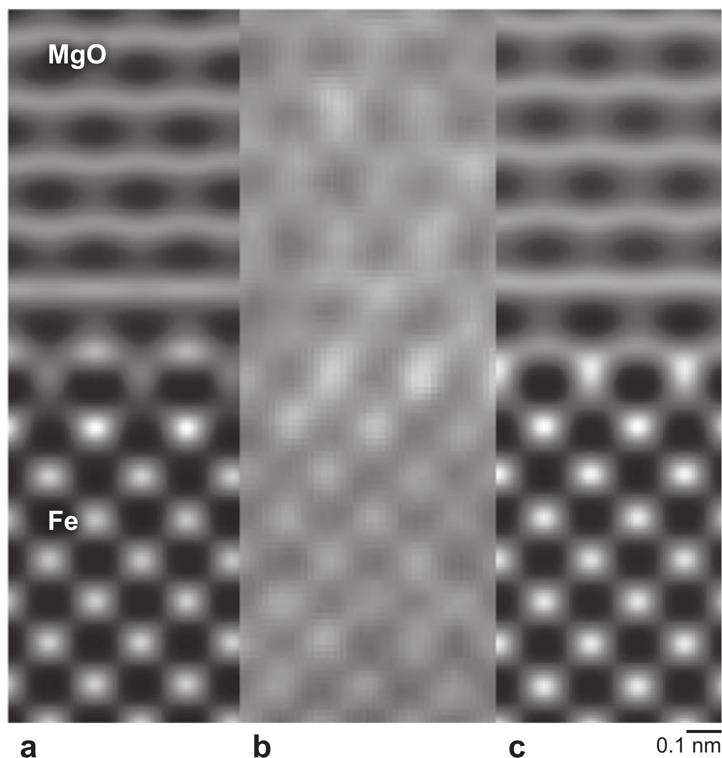

Figure 7

(*a*,*c*) Simulated images of two different interfacial models with or without a layer of FeO at the interface. (*b*) Experimental HREM image of an MgO-on-Fe interface. The model in *c* is the best fit to the experimental image and verifies a lack of a Fe-O layer at the interface. Images courtesy of C. Wang, Department of Materials, University of Oxford (105).

to reveal differences in the density of gap states for films grown by different deposition techniques. These researchers also analyzed the diffusion of B into the barrier by looking at changes in the shape of the B *K*-edge of the EELS spectrum, which enabled them to ascertain whether the B is metallic or oxidized.

Although imaging TEM and analytical TEM are useful and even required for studying the structure and chemistry of spin valves and MTJs, electron holography is unique in its ability to "image" the electric and magnetic fields associated with these types and other similar magnetoelectronic devices. Recently, electron holography has been used to investigate both the magnetization direction and fundamental electronic properties of magnetoresistive multilayers. Tanji et al. (106) have looked at Co/Cu multilayers for use in GMR applications, with varying numbers of repeat units as well as thicknesses of the nonmagnetic spacer layer. The final phase shift observed in the hologram is a superposition of the shift resulting from the magnetization as well as from the mean inner potential of the Cu and Co layers. When the mean inner potential of the metal layers is accounted for, the resulting phase shift arises solely from the magnetization of the Co layers. Tanji et al. found that the magnetization vectors of the Co layers fell into two categories: those for which the magnetization of all the magnetic layers were parallel and those for which the magnetizations were grouped in parallel/antiparallel bunches of 2–3 layers. The fact that a specimen was never observed with antiparallel alignment in every adjacent ferromagnetic layer was used to

Annu. Rev. Mater. Res. 2008.38:559-584. Downloaded from arjournals.annualreviews.org
by UNIVERSITY OF WASHINGTON - HEALTH SCIENCES LIBRARIES on 10/21/08. For personal use only.

I-V: current-voltage

explain the magnetization characteristics obtained via alternating gradient magnetometry, which indicated that the specimen did not show perfect antiferromagnetism, as expected, but instead weak ferromagnetism. Similarly, Dunin-Borkowski et al. (107) used electron holography techniques to show that the relative magnetizations of the free and pinned ferromagnetic layers in an exchange-biased AlO_x-based MTJ could be reversed from parallel to antiparallel alignment by making use of the magnetic field of the objective lens. The relatively small phase shifts associated with magnetization reversal were separated from those resulting from thickness and composition variation, demonstrating that electron holography is a powerful tool for obtaining quantitative information on the magnetization of the ferromagnetic layers in MTJs.

In another study, Wang et al. (108) used electron holography to measure the position and shape of potential wells in AlO_x-based double MTJs. Wide potential wells with varying barrier height were found in as-grown double MTJs for which the corresponding HREM images showed a diffuse and rough interface. Sharp potential wells of equal magnitude corresponded with annealed specimens whose HREM images similarly showed sharp, flat interfaces. The TMR value and general structural quality of the specimen corresponded with the degree of symmetry and sharpness of the potential well calculated from the electron hologram.

As mentioned in Section 2.6, it is common to modify the actual TEM holder or stage itself to perform in situ experiments. Electrical characterization of composition-modulated antiferroelectric $Pb_{0.99}Nb_{0.02}[(Zr_{1-x}Sn_x)_{1-y}Ti_y]_{0.98}O_3$ (PZST) ceramics has been investigated in situ in the TEM and is discussed below in Section 3.4 (109). A recent study by Chiaramonti et al. (110) combined real-time imaging with characterization of the transport properties of CoFe/MgO/CoFe MTJs (**Figure 8*a***), using a novel "nanobiasing" TEM holder designed to measure current-voltage (I-V) characteristics of specially prepared cross-section TEM specimens in situ. The study is unique in attempting to correlate site-specific transport properties with the quality of the tunneling

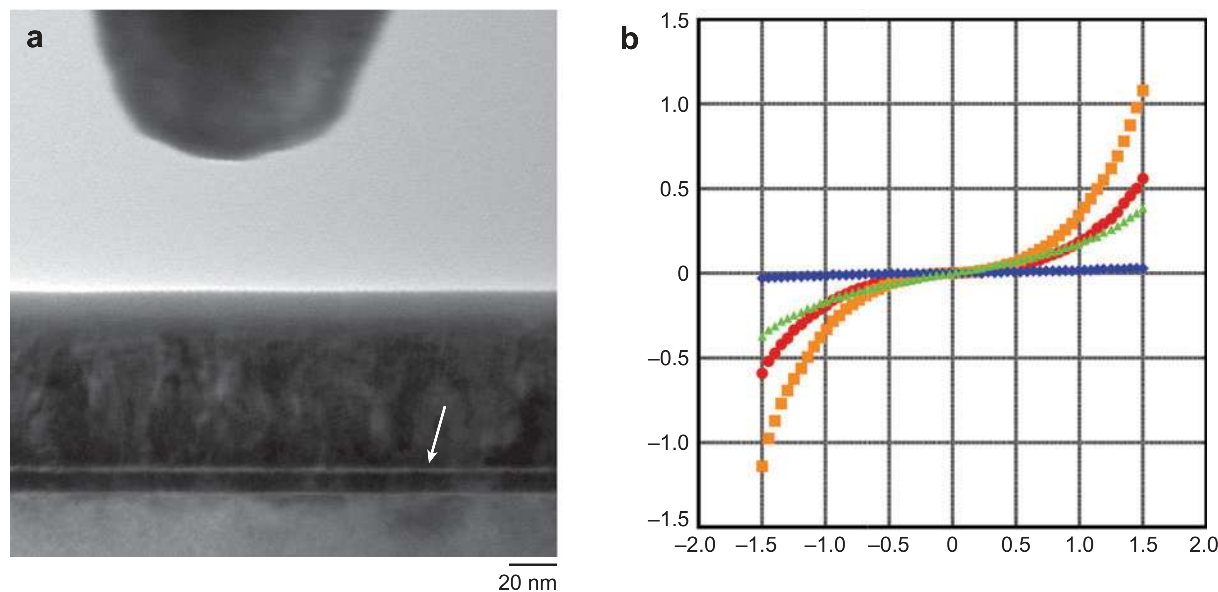

Figure 8

(*a*) TEM image of a CoFe/MgO/CoFe MTJ and gold probe tip. The MgO tunnel barrier (indicated by an *arrow*) shows pale contrast. (*b*) Four current-voltage (I-V) curves obtained in situ from the TEM sample in panel *a*, demonstrating the variability of I-V characteristics with position. Each curve was obtained from a different point along a 20-μm electron-transparent window.

Annu. Rev. Mater. Res. 2008.38:559-584. Downloaded from arjournals.annualreviews.org
by UNIVERSITY OF WASHINGTON - HEALTH SCIENCES LIBRARIES on 10/21/08. For personal use only.

barrier and its interfaces at the tunneling site via direct TEM observation. By combination of the in situ transport measurements with atom probe tomography data, the effects of interfacial mixing on transport could be determined. I-V curves such as those in **Figure 8*b*** demonstrate the sensitivity of the in situ TEM technique to the variation in transport properties caused by subtle differences in the tunnel barrier and its interfaces.

3.3. Hard Coatings

Superhard coatings based on nanometer-scale multilayers have led to the development of films with hardness values of >50 GPa, which can be considerably greater than the hardness of the equivalent monolithic material. Multilayer coatings can also show very good thermal stability, depending on the nature of the individual layers and the way in which they interact (17). The high hardness is related to the fact that the layering restricts dislocation motion, and to maintain thermal stability, the multilayer films must retain their layered microstructure, even at high temperatures. This means that such films must have well-defined interfaces with high cohesive strength and that the layers themselves must have a small grain size. As such, a good understanding of the microstructure and interface is critical to understanding the mechanical properties. For example, Lackner et al. (111) used TEM to analyze $Cr/CrN_x/CrC_xN_{1-x}$ multilayer coatings deposited by pulsed laser deposition (PLD). Data obtained using electron diffraction and EDX analysis revealed the microstructure of the layers, in terms of grain size, and also the fact that the layers incorporated oxygen from the environment of the deposition chamber, with the formation of Cr oxide phases in the nitride coating. Yamamoto et al. (112) used TEM bright-field imaging, HREM, and electron diffraction to understand the morphology of CrN/BCN multilayer coatings. Yamamoto et al. (112) also showed that the increased hardness resulted from the reduction of grain size in the CrN as a result of layering with the amorphous BCN, even though the BCN layers were only a few nanometers in thickness. A further effect of the BCN layers was to reduce dramatically the friction coefficient of the coatings, leading to much better wear behavior.

Hard coatings based on TiAlN have attracted considerable attention for high-temperature applications, and Hovsepian and colleagues (113) have made very effective use of TEM to determine the origin of the enhancement of thermal stability in TiAlCrN/TiAlYN and TiAlN/CrN nanoscale multilayer films. Bright-field images of cross-sectional samples, combined with chemical mapping using STEM-EDX, showed that the Y segregated to columnar grain boundaries running through the multilayer stack. This led to a reduction of porosity during annealing and prevented oxidation at the boundaries, improving the thermal stability and the wear resistance. A further example is the study by Wang et al. (108) in which bright-field TEM imaging and electron diffraction on cross-sectional samples were used to correlate microstructure and mechanical properties in TiN/ZrN multilayer coatings. The TEM images showed very clearly the way in which the layering process interrupts the growth of columnar grains through the whole stack, and also enabled the local phases present, and their crystallographic orientation, to be identified. The same study used XRD to show that a change in lattice parameter occurred for the thinner layers as Zr dissolved in the TiN. The critical load increased as the layer thickness decreased, as a result of maximizing the stress accommodation of the nanoscale multilayer.

Lloyd et al. (114) carried out a detailed comparison of the application of Fresnel fringe imaging, EFTEM imaging, and XRD to nanoscale TiN/NbN multilayers. Lloyd et al. (114) used the techniques to analyze the composition profile of the layers and concluded that, although XRD gave the most accurate measurement of the periodicity of the layers, Fresnel contrast imaging

Annu. Rev. Mater. Res. 2008.38:559-584. Downloaded from arjournals.annualreviews.org
by UNIVERSITY OF WASHINGTON - HEALTH SCIENCES LIBRARIES on 10/21/08. For personal use only.

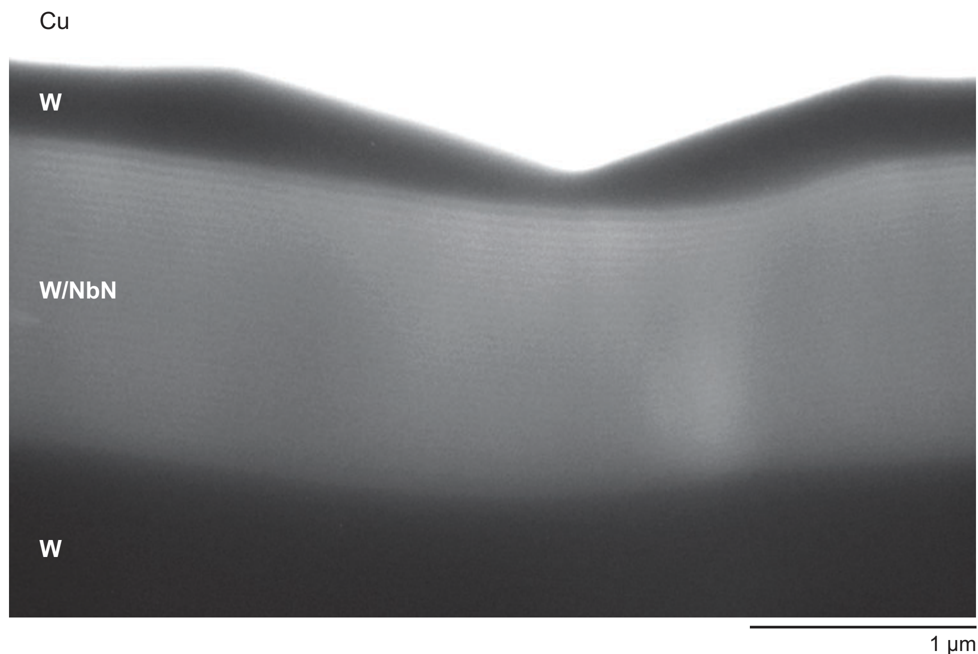

Figure 9

Cross-sectional TEM image through a W/(NbN/W)$_x$/W multilayer sample. The indentation depth is 700 nm, and the deformation of the layers under the indent can be clearly seen. Image courtesy of Dr. T. Foecke, NIST, Gaithersburg, and reprinted from Reference 115 with permission. Copyright 2004, Elsevier.

provided a more accurate measure of the composition profile and coherency strains. The authors do include the proviso, reiterated often in this paper, that the layers must be viewed edge on for the TEM-based techniques to be accurate.

In addition to providing a powerful technique for analyzing the microstructure and composition profile of as-deposited and annealed multilayer coatings, TEM has also been used to determine the deformation process that occurs in W/NbN multilayers following indentation (115). **Figure 9** shows a cross-sectional bright-field image through a nanoindent in a W/Nb multilayer specimen in which the nanoindent has led to a macroscopic shape change in the layers and W cap. Cross-sectional HREM images of the same region showed the presence of planar faults in the NbN layers, seen only under nanoindents above a certain depth. These were identified from the images as stacking faults due to the motion of partial dislocations in the layers.

3.4. All-Oxide Multilayers

Complex oxide thin films with the perovskite crystal structure have been the subject of intense research for many years because of the wide range of physical properties that they can exhibit as a function of composition. Just to name a few examples, manganite films such as $La_xCa_{1-x}MnO_3$ (LCMO) can display colossal magnetoresistance for particular compositions (116), $SrTiO_3$ (STO) is an excellent insulator, $YBa_2Cu_3O_{7-x}$ (YBCO) is a high-temperature superconductor (117), and $BaTiO_3$ is a ferroelectric material (118). High-quality perovskite superlattices are now relatively easy to grow by various methods such as metal organic chemical vapor deposition (119), MBE

Annu. Rev. Mater. Res. 2008.38:559-584. Downloaded from arjournals.annualreviews.org
by UNIVERSITY OF WASHINGTON - HEALTH SCIENCES LIBRARIES on 10/21/08. For personal use only.

(120), and PLD (21), opening up the range of functional properties that can be explored and resulting in ideal systems in which to study the interplay of the various phenomena exhibited by the component layers. For example, combining ferroelectric and magnetic perovskites in a superlattice results in multiferroic behavior that can be much better controlled than in the very few naturally occurring multiferroic materials (121), and also can lead to enhanced magnetotransport properties (122). However, in all cases the crystallinity of the layers and the nature of the interfaces in terms of roughness, interdiffusion, and interfacial strain are critical to controlling the properties and indeed can result in novel and sometimes unexpected behavior. For example, Brinkman et al. (123) recently reported the observation of ferromagnetism at the interfaces in an STO/$LaAlO_3$ (LAO) superlattice, although both STO and LAO are insulating and nonmagnetic.

Understanding the structure and chemistry of the layers, and in particular of the interfaces, is again therefore critical. TEM has been used extensively, and often in conjunction with XRD, to address this. At the simplest level, bright-field imaging, HREM, and electron diffraction have been used to analyze the thickness of layers and the epitaxial relationship between them and the substrate (see, for example, References 119, 124, and 125). However, more sophisticated TEM and STEM techniques have also been very successfully employed to elucidate the structure of perovskite superlattices. Kuwata et al. (126) used HREM, STEM dark-field imaging, and EDX analysis to study $SrZr_{0.95}Y_{0.05}O_3$/STO (SZY/STO) superlattices, which act as proton conductors and have applications in hydrogen fuel cells (127). The TEM and STEM data showed that the interfaces between the layers were smooth, although misfit dislocations were observed. In addition, no intermixing between Zr and Ti was observed. The proton conductivity of the films was considerably higher than that of a single SZY film, although the EDX analysis showed evidence for Mg diffusion from the substrate, which prevents the maximum conductivity from being achieved. The most detailed studies on perovskite superlattices have been carried out via a combination of STEM-HAADF imaging and EELS. Analysis of a $CaTiO_3/La_xCa_{1-x}TiO_3$ superlattice by Varela et al. (35) allowed the presence of a single La atom within a $CaTiO_3$ layer to be identified, and authors from the same research group have used these techniques to show that YBCO/LCMO superlattices do not have CuO chains at the interfaces, which will adversely affect their superconducting properties.

Of course, perovskite superlattices are not the only oxide multilayer films that are of interest, and TEM techniques have been widely applied to the analysis of simpler layered oxide films. For example, Chambers et al. (128) used STEM-HAADF imaging and EELS (see **Figure 10**) to show that the interfaces in CrO_2/Fe_2O_3 heterostructures were abrupt, with mixing extending no further than 1 monolayer from the interface. These data could then be input to a model from which the interface dipole potential and the band offset at the interface could be determined. In HfO_2/TiO_2 multilayer structures the band offset is also of interest because of the potential applications of these structures in charge-trapping information storage devices. Maikap et al. (129) used HREM and X-ray photoelectron spectroscopy (XPS) to analyze the interfacial abruptness in these systems and to correlate this with the charge-storage characteristics of the films. Similarly, Pennycook et al. (130) used STEM-HAADF imaging to image local atomic relaxation at the interface in NiO/ZrO_2 layered films. This relaxation can assist in the formation of Ni/ZrO_2 interfaces via electrochemical reduction, which is known to occur in these materials.

In some dielectric oxides, a ferroelectric/antiferroelectric phase transition occurs spontaneously under an applied electric field and can be exploited for energy storage, current source, and voltage filtering devices. In modified antiferroelectric oxides such as $PbZrO_3$ doped with La, Nb, Sn, or Ti, the free-energy difference between the ferroelectric and antiferroelectric states can be so small that incommensurate modulations of the two phases will form. Although these are not physically deposited layers as such, they act as multilayers and can be investigated through in situ TEM

Annu. Rev. Mater. Res. 2008.38:559-584. Downloaded from arjournals.annualreviews.org
by UNIVERSITY OF WASHINGTON - HEALTH SCIENCES LIBRARIES on 10/21/08. For personal use only.

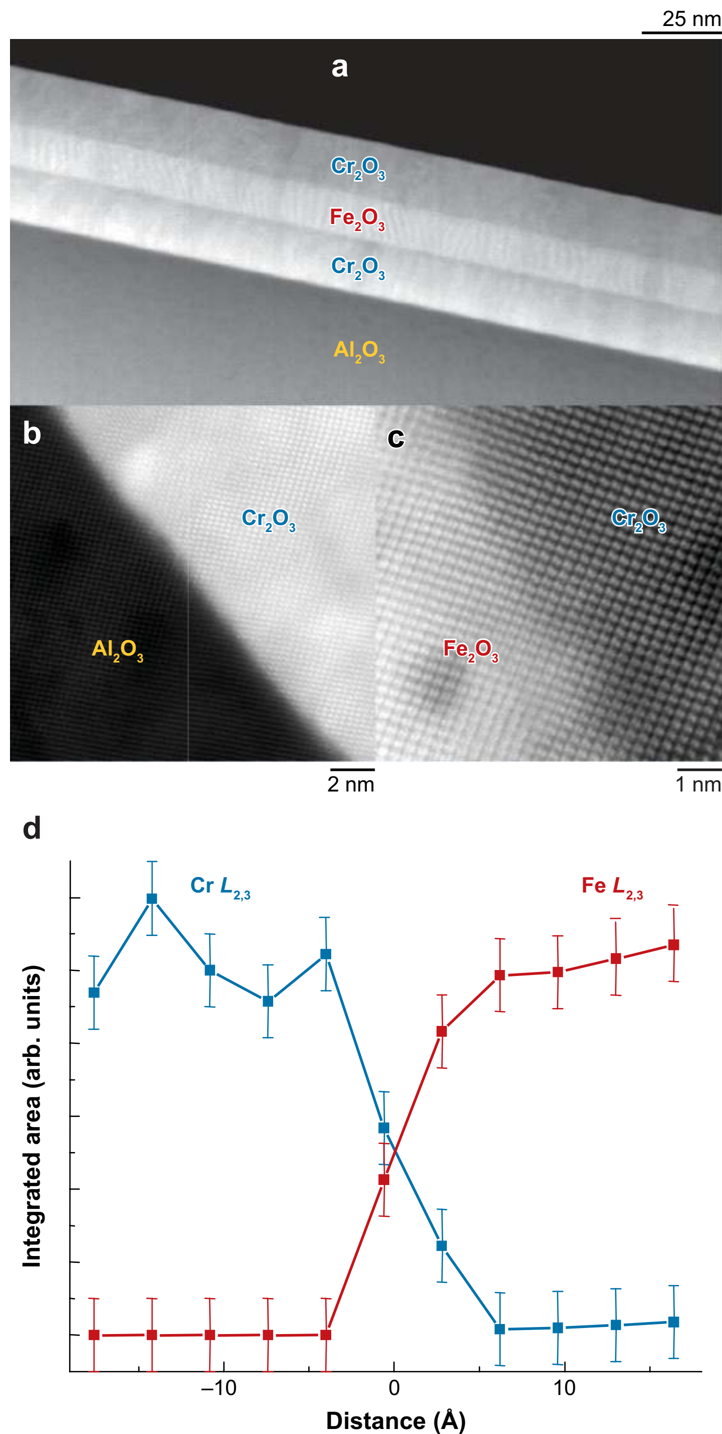

Figure 10

(*a*) Low-resolution HAADF-STEM images of the oxide multilayer, showing an apparent high degree of flatness for each film. (*b*,*c*) Higher-resolution HAADF-STEM images revealing the cation rows at each oxide interface, again suggesting a flat interface. (*d*) Integrated area under the Cr $L_{2,3}$ and Fe $L_{2,3}$ loss features as a function of distance from the interface. Energy loss spectra were taken along a line normal to the interface of α-Cr_2O_3 and α-Fe_2O_3. Images courtesy of S.A. Chambers, Pacific Northwest National Laboratory and reprinted from Reference 128 with permission. Copyright 2005, Elsevier.

techniques. Tan et al. (109) used a modified TEM stage interfaced to a high-voltage power supply that could source static and cyclic electric fields, to investigate the ferroelectric/antiferroelectric transition in PZST. Incommensurate modulated structures were detected by the presence of satellite spots in the diffraction pattern and were visualized in dark field through the use of an objective aperture large enough to include the {110}-type fundamental spot and its surrounding four satellites. Analysis of the presence and intensity of the satellite spots as a function of applied field revealed that the ferroelectric phase transformation was metastable and that the backward transformation in the grain being investigated was sluggish.

4. SUMMARY

TEM has played a critical role in unraveling the microstructural and compositional origins of the rich variety of novel behavior exhibited by multilayer thin films. The TEM techniques that have been applied to the analysis of these materials range from simple bright-field imaging to determine parameters such as layer thickness in cross section, to electron holography, used to probe the electronic structure of the multilayer film. In addition, the use of transmission electron microscopes as nanolaboratories has allowed their high spatial resolution and other unique capabilities, such as chemical analysis and the ability to "image" internal fields, to be applied to the study of the response of the films to external stimuli such as temperature or magnetic fields, thus extending the range of properties that can be analyzed by TEM. New developments in TEM are occurring rapidly, and TEM of multilayer thin films will remain an exciting area of research, both for revealing fundamental phenomena and for aiding in the integration of novel multilayer thin films into new technological applications.

DISCLOSURE STATEMENT

The authors are not aware of any biases that might be perceived as affecting the objectivity of this review.

ACKNOWLEDGMENTS

This manuscript has been created by UChicago Argonne, LLC, operator of Argonne National Lab (Argonne). Argonne, a U.S. Department of Energy Office of Science Laboratory, is operated under Contract No. DE-AC02-06CH11357. The electron microscopy for **Figure 6** and **Figure 8** was accomplished at the Electron Microscopy Center for Materials Research at Argonne.

LITERATURE CITED

1. Zhu JGJ, Park CD. 2006. Magnetic tunnel junctions. *Mater. Today* 9:36–45
2. Alferov ZI. 2001. Nobel Lecture: the double heterostructure concept and its applications in physics, electronics, and technology. *Rev. Mod. Phys.* 73:767–82
3. Li KB, Wu YH, Guo ZB, Zheng YK, Han GC, et al. 2007. Exchange coupling and its applications in magnetic data storage. *J. Nanosci. Nanotechnol.* 7:13–45
4. Baibich MN, Broto JM, Fert A, Vandau FN, Petroff F, et al. 1988. Giant magnetoresistance of (001)Fe/(001)Cr magnetic superlattices. *Phys. Rev. Lett.* 61:2472–75
5. Hertlein F, Oehr A, Hoffmann C, Michaelsen C, Wiesmann J. 2005. State-of-the-art of multilayer optics for laboratory X-ray devices. *Part. Part. Syst. Charact.* 22:378–83
6. Liu BX, Lai WS, Zhang ZJ. 2001. Solid-state crystal-to-amorphous transition in metal-metal multilayers and its thermodynamic and atomistic modeling. *Adv. Phys.* 50:367–429

Annu. Rev. Mater. Res. 2008.38:559-584. Downloaded from arjournals.annualreviews.org
by UNIVERSITY OF WASHINGTON - HEALTH SCIENCES LIBRARIES on 10/21/08. For personal use only.

7. Suhara T. 2004. *Semiconductor Laser Fundamentals (Optical Engineering)*. New York, Basel: Marcel Decker
8. Tropper AC, Hoogland S. 2006. Extended cavity surface-emitting semiconductor lasers. *Prog. Quantum Electron.* 30:1–43
9. Capasso F, Gmachl C, Sivco DL, Cho AY. 2002. Quantum cascade lasers. *Phys. Today* 55:34–40
10. Zheng TH, Li ZQ. 2005. The present status of Si/SiO_2 superlattice research into optoelectronic applications. *Superlattices Microstruct.* 37:227–47
11. Shakouri A. 2006. Nanoscale thermal transport and microrefrigerators on a chip. *Proc. IEEE* 94:1613–38
12. Dresselhaus MS, Chen G, Tang MY, Yang RG, Lee H, et al. 2007. New directions for low-dimensional thermoelectric materials. *Adv. Mater.* 19:1043–53
13. Shi LP, Chong TC. 2007. Nanophase change for data storage applications. *J. Nanosci. Nanotechnol.* 7:65–93
14. Ziebert C, Ulrich S. 2006. Hard multilayer coatings containing TiN and/or ZrN: a review and recent progress in their nanoscale characterization. *J. Vac. Sci. Technol. A* 24:554–83
15. Sproul WD. 1994. Multilayer, multicomponent, and multiphase physical vapor-deposition coatings for enhanced performance. *J. Vac. Sci. Technol. A* 12:1595–601
16. Setoyama M, Nakayama A, Tanaka M, Kitagawa N, Nomura T. 1996. Formation of cubic-AlN in TiN/AlN superlattice. *Surf. Coat. Technol.* 86:225–30
17. Raveh A, Zukerman I, Shneck R, Avni R, Fried I. 2007. Thermal stability of nanostructured superhard coatings: a review. *Surf. Coat. Technol.* 201:6136–42
18. Zheng YK, Wu YH, Li KB, Qiu JJ, Han GC, et al. 2007. Magnetic random access memory (MRAM). *J. Nanosci. Nanotechnol.* 7:117–37
19. Scott JF. 2006. Nanoferroelectrics: statics and dynamics. *J. Phys. Condens. Matter* 18:R361–86
20. Jayadevan KP, Tseng TY. 2002. Composite and multilayer ferroelectric thin films: processing, properties and applications. *J. Mater. Sci. Mater. Electron.* 13:439–59
21. Ijiri Y. 2002. Coupling and interface effects in magnetic oxide superlattices. *J. Phys. Condens. Matter* 14:R947–66
22. Sree Harsha KS. 2006. *Principles of Vapor Deposition of Thin Films*. Oxford, UK: Elsevier
23. Elers KE, Blomberg T, Peussa M, Aitchison B, Haukka S, Marcus S. 2006. Film uniformity in atomic layer deposition. *Chem. Vapor Depos.* 12:13–24
24. Bass J, Pratt WP. 2007. Spin-diffusion lengths in metals and alloys, and spin-flipping at metal/metal interfaces: an experimentalist's critical review. *J. Phys. Condens. Matter* 19:183201
25. Fitzsimmons MR, Bader SD, Borchers JA, Felcher GP, Furdyna JK, et al. 2004. Neutron scattering studies of nanomagnetism and artifically structured materials. *J. Magn. Magn. Mater.* 271:103–46
26. Zabel H. 1994. X-ray and neutron reflectivity analysis of thin-films and superlattices. *Appl. Phys. A* 58:159–68
27. Fewster PF. 1996. X-ray analysis of thin films and multilayers. *Rep. Prog. Phys.* 59:1339–407
28. Kelly TF, Miller MK. 2007. Atom probe tomography. *Rev. Sci. Instrum.* 78:031101:1–20
29. Williams DB, Carter CB. 1996. *Transmission Electron Microscopy: A Textbook for Materials Science*. New York: Plenum
30. Hirsch P, Howie A, Nicholson R, Pashley DW, Whelan MJ. 1977. *Electron Microscpy of Thin Crystals*. Malabar, FL: Robert E. Krieger Publ.
31. Edington JW. 1974. *Monographs in Practical Electron Microscopy in Materials Science*. London: Macmillan
32. De Graef M. 2003. *Introduction to Conventional Transmission Electron Microscopy*. Cambridge, UK: Cambridge Univ. Press
33. Spence JCH. 1988. *Experimental High-Resolution Electron Microscopy*. New York: Oxford Univ. Press
34. Shindo D, Hiraga K. 1998. *High-Resolution Electron Microscopy for Materials Science*. Tokyo: Springer
35. Varela M, Findlay SD, Lupini AR, Christen HM, Borisevich AY, et al. 2004. Spectroscopic imaging of single atoms within a bulk solid. *Phys. Rev. Lett.* 92:095502
36. Wang S, Borisevich AY, Rashkeev SN, Glazoff MV, Sohlberg K, et al. 2004. Dopants adsorbed as single atoms prevent degradation of catalysts. *Nat. Mater.* 3:143–46
37. Peng L-M, Dudarev SL, Whelan MJ. 2004. *High-Energy Electron Diffraction and Microscopy*. New York: Oxford Univ. Press

Annu. Rev. Mater. Res. 2008.38:559-584. Downloaded from arjournals.annualreviews.org
by UNIVERSITY OF WASHINGTON - HEALTH SCIENCES LIBRARIES on 10/21/08. For personal use only.

Annu. Rev. Mater. Res. 2008.38:559-584. Downloaded from arjournals.annualreviews.org
by UNIVERSITY OF WASHINGTON - HEALTH SCIENCES LIBRARIES on 10/21/08. For personal use only.

38. Nellist PD, Pennycook SJ. 2000. The principles and interpretation of annular dark-field Z-contrast imaging. *Adv. Imaging Electron. Phys.* 113:147–203
39. Cowley JM. 1969. Image contrast in a transmission scanning electron microscope. *Appl. Phys. Lett.* 15:58–59
40. Saijo H, Nakagawa M, Yamada M, Hsu J-T, Tu R-C, et al. 2004. High-resolution scanning electron microscopy observation of GaN/AlGaN strained-layer superstructures in GaN-based violet lasers. *Jpn. J. Appl. Phys.* 43:968–69
41. Bals S, Kabius BC, Haider M, Radmilovic V, Kisielowski C. 2004. Annular dark field imaging in a TEM. *Solid State Commun.* 130:675–80
42. Brydson R. 2001. *Elecron Energy Loss Spectroscopy*. Oxford, UK: BIOS Sci. Publ.
43. Amelinckx S, van Dyck D, van Landuyt J, van Tendeloo G. 1997. *Handbook of Microscopy; Methods I*. Weinheim: VCH Verlagsgesellschaft mbH
44. Browning ND, Chisholm MF, Pennycook SJ. 1993. Atomic-resolution chemical analysis using a scanning transmission electron microscope. *Nature* 366:143–46
45. Cha JJ, Read JC, Buhrman RA, Muller DA. 2007. Spatially resolved electron energy-loss spectroscopy of electron-beam grown and sputtered CoFeB/MgO/CoFeB magnetic tunnel junctions. *Appl. Phys. Lett.* 91:062516
46. Müllejans H, Bruley J. 1994. Improvements in detection sensitivity by spatial difference electron energy-loss spectroscopy at interfaces in ceramics. *Ultramicroscopy* 53:351–60
47. Gao M, Scheu C, Tchernychova E, Rühle M. 2003. Successful application of the spatial difference technique to electron energy-loss spectroscopy studies of Mo/$SrTiO_3$ interfaces. *J. Microsc. (Oxford)* 210:94–101
48. Sigle W. 2005. Analytical transmission electron microscopy. *Annu. Rev. Mater. Res.* 35:239–314
49. Shang P, Petford-Long AK, Nickel JH, Sharma M, Anthony TC. 2001. EELS and HREM study of tunneling junctions with AlN and AlON barriers. *Inst. Phys. Conf. Ser.* 168:457–60
50. Mankos M, Scheinfein MR, Cowley JM. 1996. Quantitative micromagnetics: electron holography of magnetic thin films and multilayers. *IEEE Trans. Magn.* 32:4150–55
51. Sinkler W, Marks LD. 1999. Dynamical direct methods for everyone. *Ultramicroscopy* 75:251–68
52. Völkl E, Allard LF, Joy DC. 1999. *Introduction to Electron Holography*. New York: Kluwer Acad./Plenum Publ.
53. Dunin-Borkowski RE, McCartney MR, Smith DJ. 2004. Electron holography of nanostructured materials. In *Encyclopedia of Nanoscience and Nanotechnology, Volume 3*, ed. HS Nalwa, pp. 41–99. Stevenson Ranch: Am. Sci. Publ.
54. McCartney MR, Dunin-Borkowski RE, Smith DJ. 2001. Electron holography and its application to magnetic materials. In *Magnetic Imaging and its Applications to Materials*, ed. M De Graef, Y Zhu, pp. 111–36. San Diego: Academic
55. Paganin D, Nugent KA. 1998. Noninterferometric phase imaging with partially coherent light. *Phys. Rev. Lett.* 80:2586–89
56. De Graef M. 2001. Lorentz microscopy: theoretical basis and image simulations. In *Magnetic Imaging and its Applications to Materials*, ed. M De Graef, Y Zhu, pp. 27–67. San Diego: Academic
57. Barty A, Paganin D, Nugent KA. 2001. Phase retrieval in Lorentz microscopy. In *Magnetic Imaging and its Applications to Materials*, ed. M De Graef, Y Zhu, pp. 137–66. San Diego: Academic
58. Ishizuka K, Allman B. 2005. Phase measurement of atomic resolution image using transport of intensity. *J. Electron Microsc.* 54:191–97
59. Sinclair R, Konno TJ, Hong Ko D. 1994. TEM and in situ HREM for studying metal-semiconductor interfacial reactions. In *Reactive Phase Formation at Interfaces and Diffusion Processes*, ed. Y Limoge, 155–56:111–20. Trans Tech Publ.
60. Wang C-Y, Dohrmann JK, Bottcher C, Bahnemann DW. 2004. In-situ electron microscopy investigation of Fe(111)-doped TiO_2 nanoparticles in an aqueous environment. *J. Nanopart. Res.* 6:119–22
61. Foecke T, Kramer DE. 2003. In situ TEM observations of fracture in nanolaminated metallic thin films. *Int. J. Fract.* 119:351–57
62. Haque MA, Saif MTA. 2002. In-situ tensile testing of nano-scale specimens in SEM and TEM. *Exp. Mech.* 42:123–28

Annu. Rev. Mater. Res. 2008.38:559-584. Downloaded from arjournals.annualreviews.org
by UNIVERSITY OF WASHINGTON - HEALTH SCIENCES LIBRARIES on 10/21/08. For personal use only.

63. Warren OL, Shan Z, Syed Asif SA, Stach EA, Morris JW, Minor AM. 2007. In situ nanoindentation in the TEM. *Mater. Today* 10:59–60
64. Buckett MI, Stranes J, Luzzi DE, Zhang JP, Wessels BW, Marks LD. 1989. Electron-irradiation damage in oxides. *Ultramicroscopy* 29:217–27
65. Wang YG, Petford-Long AK. 2002. Magnetization reversal of the ferromagnetic layer in IrMn/CoFe bilayers. *J. Appl. Phys.* 92:6699–707
66. Boyes ED, Gai PL. 1997. Environmental high resolution electron microscopy and applications to chemical science. *Ultramicroscopy* 67:219–32
67. Tromp RM, Ross FM. 2000. Advances in in situ ultra-high vacuum electron microscopy: growth of SiGe on Si. *Annu. Rev. Mater. Sci.* 30:431–49
68. Xiu K, Gibson JM. 2001. Study of quadrupole C_c corrector for the large-gap HREM. *Optik* 112:521–30
69. LaGrange T, Armstrong MR, Boyden K, Brown CG, Campbell GH, et al. 2006. Single-shot dynamic transmission electron microscopy. *Appl. Phys. Lett.* 89:044105
70. Petford-Long AK, Chapman JN. 2005. Lorentz microscopy. In *Magnetic Microscopy of Nanostructures*, ed. H Hopster, HP Oepen, pp. 67–86. Berlin, Heidelberg: Springer
71. Petroff PM. 1977. Transmission electron microscopy of interfaces in III-V compound semiconductors. *J. Vac. Sci. Technol.* 14:973–78
72. Ruterana P, Ganiere JD, Buffat PA. 1988. Transmission electron microscopy of cleavage wedges: application to GaAlAs/GaAs system study. *J. Microsc. Spectrosc. Electron.* 13:421–37
73. Oshinowo J, Forchel A, Ganiere JD, Ruterana P, Stadelmann PA, et al. 1993. Investigation of GaInAs/InP interdiffusion by simultaneous transmission electron microscopy and photoluminescence analysis. *Mater. Sci. Eng. B* 21:277–80
74. Leifer K, Buffat PA, Cagnon J, Kapon E, Rudra A, Stadelmann PA. 2002. Quantitative imaging of InGaAs/GaAs layers using transmission electron microscopy methods: characterization of stresses and chemical composition. *J. Cryst. Growth* 237–39:1471–75
75. Spycher R, Buffat PA, Stadelmann PA, Roentgen P, Heuberger W, Graf V. 1989. Electron microscopy study of GaInAs/InP and GaInAsP/InP multilayer heterostructures. *Inst. Phys. Conf. Ser.* 100:299–304
76. Stadelmann PA. 1987. EMS: a software package for electron-diffraction analysis and HREM image simulation in materials science. *Ultramicroscopy* 21:131–45
77. Schneider R. 2002. High-resolution analytical TEM of nanostructured materials. *Anal. Bioanal. Chem.* 374:639–45
78. Gao M, Bradley ST, Cao Y, Jena D, Lin Y, et al. 2006. Compositional modulation and optical emission in AlGaN epitaxial films. *J. Appl. Phys.* 100:103512
79. Schmidt OG, Eberl K. 2001. Nanotechnology: thin solid films rolled up into nanotubes. *Nature* 410:168
80. Deneke C, Sigle W, Eigenthaler U, van Aken PA, Schutz G. 2007. Interfaces in semiconductor/metal radial superlattices. *Appl. Phys. Lett.* 90:263107
81. Kubel C, Voigt A, Schoenmakers R, Otten M, Su D, et al. 2005. Recent advances in electron tomography: TEM and HAADF-STEM tomography for materials science and semiconductor applications. *Microsc. Microanal.* 11:378–400
82. Gribelyuk MA, Cabral C, Gusev EP, Narayanan V. 2007. Interfacial microstructure of $NiSi_x/HfO_2/SiO_x/Si$ gate stacks. *Thin Solid Films* 515:5308–13
83. Petford-Long AK, Booker GR, Hockly M. 1989. The use of high-resolution electron-microscopy and image simulation to determine the sharpness of InP/GaInAs interfaces in multiple quantum-well structures. *Ultramicroscopy* 31:385–98
84. Lentzen M, Jahnen B, Jia CL, Thust A, Tillman K, Urban K. 2002. High-resolution imaging with an aberration-corrected transmission electron microscope. *Ultramicroscopy* 92:233–42
85. Smeeton TM, Kapers MJ, Barnard JS, Vickers ME, Humphreys CJ. 2003. Electron-beam induced strain within InGaN quantum wells: false indium "cluster" detection in the transmission electron microscope. *Appl. Phys. Lett.* 83:5419–21
86. McCartney MR, Ponce FA, Cai J, Bour DP. 2000. Mapping electrostatic potential across an AlGaN/InGaN/AlGaN diode by electron holography. *Appl. Phys. Lett.* 76:3055–57
87. Twitchett AC, Dunin-Borkowski RE, Midgley PA. 2002. Quantitative electron holography of biased semiconductor devices. *Phys. Rev. Lett.* 88:238302

Annu. Rev. Mater. Res. 2008.38:559-584. Downloaded from arjournals.annualreviews.org
by UNIVERSITY OF WASHINGTON - HEALTH SCIENCES LIBRARIES on 10/21/08. For personal use only.

88. Dieny B, Speriosu VS, Mtin S, Parkin SSP, Gurney BA, et al. 1991. Magnetotransport properties of magnetically soft spin-valve structures. *J. Appl. Phys.* 69:4774–79
89. Moodera JS, Kinder LR, Wong TM, Meservey R. 1995. Large magnetoresistance at room-temperature in ferromagnetic thin-film tunnel-junctions. *Phys. Rev. Lett.* 74:3273–76
90. Tsymbal EY, Pettifor DG. 2001. Perspectives of giant magnetoresistance. *Solid State Phys. Adv. Res. Appl.* 56:113–237
91. Portier X, Petford-Long AK. 1999. Electron microscopy studies of spin-valve materials. *J. Phys. D* 32:R89–108
92. Song SA, Hirano T, Park JB, Kaji K, Kim KH, Terada S. 2005. Searching ultimate nanometrology for AlO_x thickness in magnetic tunnel junction by analytical electron microscopy and X-ray reflectometry. *Microsc. Microanal.* 11:431–45
93. Portier X, Petford-Long AK, Bayle-Guillemaud P, Anthony TC, Brug JA. 1999. HREM study of the 'orange-peel' effect in spin valves. *J. Magn. Magn. Mater.* 198–99:110–12
94. Rouvière JL. 1994. Characterization of interfaces by HREM. What can we get with quantitative analysis? *Proc. ICEM 13* 2A:123–26
95. Neel L. 1962. Sur un problème de magnétostatique relatif à des couches minces ferromagnétiques. *C.R. Hebd. Seances Acad. Sci.* 255:1545–50
96. Butler WH, Zhang X-G, Schulthess TC, MacLaren JM. 2001. Spin-dependent tunneling conductance of Fe/MgO/Fe sandwiches. *Phys. Rev. B* 63:054416
97. Parkin SSP, Kaiser C, Panchula A, Rice PM, Hughes B, et al. 2004. Giant tunneling magnetoresistance at room temperature with MgO (100) tunnel barriers. *Nat. Mater.* 3:862–67
98. Yuasa S, Nagahama T, Fukushima A, Suzuki Y, Ando K. 2004. Giant room-temperature magnetoresistance in single-crystal Fe/MgO/Fe magnetic tunnel junctions. *Nat. Mater.* 3:868–71
99. Djayaprawira DD, Tsunekawa K, Nagai M, Maehara H, Yamagata S, Watanabe N. 2005. 230% room-temperature magnetoresistance in CoFeB/MgO/CoFeB magnetic tunnel junctions. *Appl. Phys. Lett.* 86:092502
100. Lee YM, Hayakawa J, Ikeda S, Matsukura F, Ohno H. 2006. Giant tunnel magnetoresistance and high annealing stability in CoFeB/MgO/CoFeB magnetic tunnel junctions with synthetic pinned layer. *Appl. Phys. Lett.* 89:042506
101. Tsymbal EY, Mryasov ON, LeClair PR. 2003. Spin-dependent tunneling in magnetic tunnel junctions. *J. Phys. Condens. Matter* 15:R109–42
102. Miller CW, Li Z-P, Schuller IK, Dave RW, Slaughter JM, Akerman J. 2006. Origin of the breakdown of Wentzel-Kramers-Brillouin-based tunneling models. *Phys. Rev. B* 74:212404
103. Meyerheim HL, Popescu R, Jedrecy N, Vedpathak V, Sauvage-Simkin M, et al. 2002. Surface X-ray diffraction analysis of the MgO/Fe(001) interface: evidence for an FeO layer. *Phys. Rev. B* 65:144433
104. Miyokawa K. 2005. X-ray absorption and X-ray magnetic circular dichroism of a monatomic Fe(001) layer facing a single-crystalline MgO(001) tunnel barrier. *Jpn. J. Appl. Phys.* 44:L9–11
105. Wang C, Wang S, Kohn A, Ward RCC, Petford-Long AK. 2007. Transmission electron microscopy study of the Fe(001)|MgO(001) interface for magnetic tunnel junctions. *IEEE Trans. Magn.* 43:2779–81
106. Tanji T, Hasebe S, Suzuki T. 2002. Holographic observation of magnetic fine-structures in new magnetic materials. *Microsc. Microanal.* 8:30–31
107. Dunin-Borkowski RE, McCartney MR, Smith DJ, Parkin SSP. 1998. Towards quantitative electron holography of magnetic thin films using in-situ magnetization reversal. *Ultramicroscopy* 74:61–73
108. Wang IY, He JL, Chen KC, Davison A. 2006. Nano-multilayer Ti-Zr-N coating by a central configured multi-arc coating process. *Surf. Coat. Technol.* 201:4174–79
109. Tan X, He H, Shang J-K. 2005. In-situ transmission electron microscopy studies of electric-field-induced phenomena in ferroelectrics. *J. Mater. Res.* 20:1641–53
110. Chiaramonti AN, Schreiber DK, Kabius BC, Egelhoff WF, Petford-Long AK. 2007. In-situ structure and transport correlations in magnetic tunnel junctions. *Microsc. Microanal.* 13:626–27CD
111. Lackner JM, Waldhauser W, Major B, Morgiel J, Major L, et al. 2006. Growth structure and growth defects in pulsed laser deposited Cr-CrN_x-CrC_xN_{1-x} multilayer coatings. *Surf. Coat. Technol.* 200:3644–49

Annu. Rev. Mater. Res. 2008.38:559-584. Downloaded from arjournals.annualreviews.org
by UNIVERSITY OF WASHINGTON - HEALTH SCIENCES LIBRARIES on 10/21/08. For personal use only.

112. Yamamoto K, Ito H, Kujime S. 2007. Nano-multilayered CrN/BCN coating for antiwear and low friction applications. *Surf. Coat. Technol.* 201:5244–48
113. Zhou Z, Rainforth WM, Falke U, Falke M, Bleloch A, Hovsepian PE. 2007. On the structure and composition of nanoscale TiAlN/VN multilayers. *Philos. Mag.* 87:967–78
114. Lloyd SJ, Molina-Aldareguia JM, Clegg WJ. 2005. Structural characterization of TiN/NbN multilayers: X-ray diffraction, energy-filtered TEM and Fresnel contrast techniques compared. *J. Microsc. (Oxford)* 217:241–59
115. Kramer DE, Savage MF, Lin A, Foecke T. 2004. Novel method for TEM characterization of deformation under nanoindents in nanolayered materials. *Scripta Mater.* 50:745–49
116. von Helmolt R, Wecker J, Holzapfel B, Schultz L, Samwer K. 1993. Giant negative magnetoresistance in perovskitelike $La_{2/3}Ba_{1/3}MnO_x$ ferromagnetic films. *Phys. Rev. Lett.* 71:2331–33
117. Wu MK, Ashburn JR, Torng CJ, Hor PH, Meng RL, et al. 1987. Superconductivity at 93K in a new mixed-phase Y-Ba-Cu-O compound system at ambient pressure. *Phys. Rev. Lett.* 58:908–10
118. Setter N, Damjanovic D, Eng L, Fox G, Gevorgian S, et al. 2006. Ferroelectric thin films: review of materials, properties, and applications. *J. Appl. Phys.* 100:051606
119. Weiss F, Lindner J, Senateur JP, Dubourdieu C, Galindo V, et al. 2000. Injection MOCVD: ferroelectric thin films and functional oxide superlattices. *Surf. Coat. Technol.* 133:191–97
120. Schlom DG, Haeni JH, Lettieri J, Theis CD, Tian W, et al. 2001. Oxide nano-engineering using MBE. *Mater. Sci. Eng. B* 87:282–91
121. Singh MP, Prellier W. 2007. Oxide superlattices for multiferroics: opportunities, issues, and challenges. *Philos. Mag. Lett.* 87:211–22
122. Murugavel P, Padhan P, Prellier W. 2004. Enhanced magnetoresistance in ferromagnetic $Pr_{0.85}Ca_{0.15}MnO_3$/ferroelectric $Ba_{0.6}Sr_{0.4}TiO_3$ superlattice films. *Appl. Phys. Lett.* 85:4992–94
123. Brinkman A, Huijben M, Van Zalk M, Huijben J, Zeitler U, et al. 2007. Magnetic effects at the interface between nonmagnetic oxides. *Nat. Mater.* 6:493–96
124. Wang ZY, Yasuda T, Hatatani S, Oda S. 1999. Enhanced dielectric properties in $SrTiO_3/BaTiO_3$ strained superlattice structures prepared by atomic-layer metalorganic chemical vapor deposition. *Jpn. J. Appl. Phys. Pt. 1* 38:6817–20
125. Kim BR, Kim TU, Lee WJ, Moon JH, Lee BT, et al. 2007. Effects of periodicity and oxygen partial pressure on the crystallinity and dielectric property of artificial $SrTiO_3/BaTiO_3$ superlattices integrated on Si substrates by pulsed laser deposition method. *Thin Solid Films* 515:6438–41
126. Kuwata N, Sata N, Saito S, Tsurui T, Yugami H. 2006. Structural and electrical properties of $SrZr_{0.95}Y_{0.05}O_3/SrTiO_3$ superlattices. *Solid State Ionics* 177:2347–51
127. Kreuer KD. 2003. Proton-conducting oxides. *Annu. Rev. Mater. Res.* 33:333–59
128. Chambers SA, Williams JR, Henderson MA, Joly AG, Varela M, Pennycook SJ. 2005. Structure, band offsets and photochemistry at epitaxial alpha-Cr_2O_3/alpha-Fe_2O_3 heterojunctions. *Surf. Sci.* 587:L197–207
129. Maikap S, Wang T-Y, Tzeng P-J, Lin C-H, Tien TC, et al. 2007. Band offsets and charge storage characteristics of atomic layer deposited high-*k* HfO_2/TiO_2 multilayers. *Appl. Phys. Lett.* 90:262901
130. Dickey EC, Dravid VP, Nellist PD, Wallis DJ, Pennycook SJ, Revcolevschi A. 1997. Structure and bonding at Ni-ZrO_2 (cubic) interfaces formed by the reduction of a NiO-ZrO_2 (cubic) composite. *Microsc. Microanal.* 3:443–50

Annual Review of Materials Research

Volume 38, 2008

Contents

Annu. Rev. Mater. Res. 2008.38:559-584. Downloaded from arjournals.annualreviews.org by UNIVERSITY OF WASHINGTON - HEALTH SCIENCES LIBRARIES on 10/21/08. For personal use only.

Low- and High-Temperature Wetting: State of the Art

Wetting and Molecular Dynamics Simulations of Simple Liquids
J. De Coninck and T.D. Blake 1

Dynamics of Wetting from an Experimental Point of View
John Ralston, Mihail Popescu, and Rossen Sedev 23

Anisotropy of Wetting
Dominique Chatain 45

Wetting and Roughness
David Quéré 71

Wetting and Dewetting of Complex Surface Geometries
Stephan Herminghaus, Martin Brinkmann, and Ralf Seemann 101

Modeling of Wetting in Restricted Geometries
Kurt Binder 123

Wetting Phenomena in Nanofluidics
M. Rauscher and S. Dietrich 143

Interfacial Segregation Effects in Wetting Phenomena
Paul Wynblatt 173

High-Temperature Wetting and the Work of Adhesion in Metal/Oxide Systems
Eduardo Saiz, Rowland M. Cannon, and Antoni P. Tomsia 197

Wetting and Prewetting on Ceramic Surfaces
Jian Luo and Yet-Ming Chiang 227

Wetting in Soldering and Microelectronics
T. Matsumoto and K. Nogi 251

Segregation Phenomena at Thermally Grown Al_2O_3/Alloy Interfaces
P.Y. Hou 275

Annu. Rev. Mater. Res. 2008.38:559-584. Downloaded from arjournals.annualreviews.org
by UNIVERSITY OF WASHINGTON - HEALTH SCIENCES LIBRARIES on 10/21/08. For personal use only.

Current Interest

Combinatorial Materials Sciences: Experimental Strategies for Accelerated Knowledge Discovery
Krishna Rajan 299

Bamboo and Wood in Musical Instruments
Ulrike G.K. Wegst 323

Controlled Patterning of Ferroelectric Domains: Fundamental Concepts and Applications
Dongbo Li and Dawn A. Bonnell 351

Crystal Chemistry of Complex Perovskites: New Cation-Ordered Dielectric Oxides
P.K. Davies, H. Wu, A.Y. Borisevich, I.E. Molodetsky, and L. Farber 369

Formation and Properties of Quasicrystals
D.V. Louzguine-Luzgin and A. Inoue 403

Integral Textile Ceramic Structures
David B. Marshall and Brian N. Cox 425

Mechanical Behavior of Metallic Glasses: Microscopic Understanding of Strength and Ductility
Mingwei Chen 445

Recent Developments in Irradiation-Resistant Steels
G.R. Odette, M.J. Alinger, and B.D. Wirth 471

Trends in the Development of New Mg Alloys
M. Bamberger and G. Dehm 505

The Theory and Interpretation of Electron Energy Loss Near-Edge Fine Structure
Peter Rez and David A. Muller 535

Transmission Electron Microscopy of Multilayer Thin Films
Amanda K. Petford-Long and Ann N. Chiaramonti 559

Index

Cumulative Index of Contributing Authors, Volumes 34–38 585

Errata

An online log of corrections to *Annual Review of Materials Research* articles may be found at http://matsci.annualreviews.org/errata.shtml